2005
Annual Progress Report

AUTOMOTIVE PROPULSION MATERIALS

Less dependence on foreign oil, and eventual transition to an emissions-free, petroleum-free vehicle

FREEDOMCAR AND VEHICLE TECHNOLOGIES PROGRAM

U.S. Department of Energy
Energy Efficiency and Renewable Energy
Bringing you a prosperous future where energy is clean, abundant, reliable, and affordable

FreedomCAR & Fuel Partnership

21st CENTURY TRUCK PARTNERSHIP

Acknowledgment

We would like to thank our program participants for their contributions to the programs, and all the authors who prepared the project abstracts that make up this report. In addition, we would like to express our sincere appreciation to Brenda Hickey for compiling this report and to Deborah Counce and Brenda Phillips for their contributions in preparing and publishing it.

U.S. Department of Energy
Office of FreedomCAR and Vehicle Technologies
1000 Independence Avenue S.W.
Washington, DC 20585-0121

FY 2005

Progress Report for Automotive Propulsion Materials Program

Energy Efficiency and Renewable Energy
Office of FreedomCAR and Vehicle Technologies

Edward Wall
Program Manager

December 2005

CONTENTS

1. INTRODUCTION

Automotive Propulsion Materials R&D: Enabling Technologies to Meet FreedomCAR Program Goals

The Department of Energy's (DOE's) Office of FreedomCAR and Vehicle Technologies (OFCVT) is pleased to introduce the FY 2005 *Annual Progress Report for the Automotive Propulsion Materials Research and Development Program*. Together with DOE national laboratories and in partnership with private industry and universities across the United States, the program continues to engage in research and development (R&D) that provides enabling materials technology for fuel-efficient and environmentally friendly light-duty vehicles.

This introduction summarizes the objectives, progress, and highlights of the program in FY 2005. It also describes the technical barriers remaining and the future direction of the program. The FY 2005 annual progress reports on *Combustion and Emission Control for Advanced CIDI Engines* and *Power Electronics* provide additional information on OFCVT's R&D activities that support the development of propulsion materials technology.

In August of 2005, President Bush signed the Energy Policy Act of 2005. This comprehensive energy policy specifically addresses the development of energy-efficient vehicle technologies, including hybrid systems, advanced emission control technologies, fuel cells, and hydrogen-based systems. The Energy Policy Act is a strong indicator of the continuing federal support for advanced automotive technologies and the materials work that supports them.

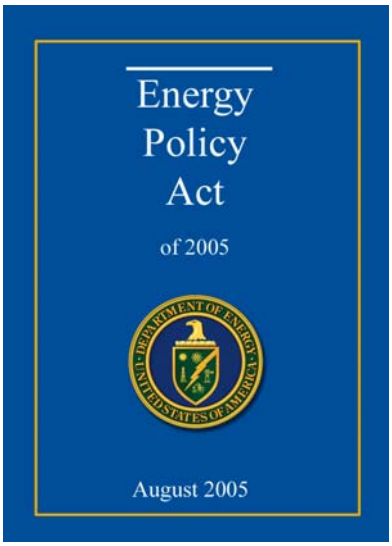

The Automotive Propulsion Materials (APM) R&D Program has supported the FreedomCAR Program since its inception. FreedomCAR is not an automobile or prototype but rather a new approach to developing the technologies for vehicles of the future. In research areas where industry views the risks as too high and uncertain, the FreedomCAR Program conducts long-term research, development, and demonstration activities that bring the technology to a stage of maturity such that industry can undertake the final commercialization stages.

The APM Program is a partner with the OFCVT programs for Power Electronics and Electric Machines and for Combustion and Emissions Control for Advanced CIDI Engines. Projects within the APM Program address materials concerns that directly impact the critical technical barriers in each of these programs—barriers such as thermal management, emissions reduction, and reduced manufacturing costs. The program engages only the barriers that involve fundamental, high-risk materials issues.

Enabling Technologies

The APM Program focuses on enabling materials technologies that are critical in removing barriers to the power electronics and compression-ignition, direct-injection (CIDI) engine and emissions control research programs. The program supports these two core technology areas by providing materials expertise, testing capabilities, and technical solutions for materials problems. The component development, materials processing, and characterization that the program provides are enablers of the successful development of efficient electric drive systems and emissions-compliant CIDI engines.

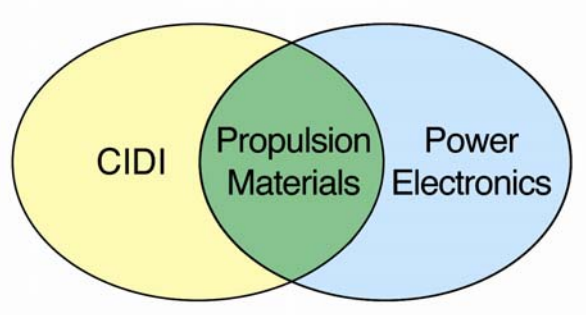

The Propulsion Materials Program focuses on two applications.

Thermal management is a crosscutting engineering issue that affects both the power electronics and CIDI programs. The components necessary for high-fuel-economy, low-emission hybrid electric and fuel cell vehicles require that power electronics be smaller and lighter and operate at higher temperatures than those for conventional vehicles. These requirements are being addressed by developing electronic materials (i.e., materials for low-cost dc bus capacitors) that operate at higher temperatures and by improving the capability to dissipate heat generated in electronic devices. The APM Program has been addressing electric drive system heat dissipation issues through the development of advanced carbon foam technology.

Current CIDI engines must strike a delicate balance between high efficiency and low tailpipe emissions. CIDI engine and aftertreatment system development will greatly benefit from the Program's efforts to develop improved engine components and subsystems. The APM Program featured a project to develop technology to produce very small (~50 micron) orifices for fuel injectors used in high-pressure common rail systems. The smaller orifices can enable better control of fuel atomization that will increase efficiency and reduce emissions. An exploratory study was initiated in FY 2004 at Pacific Northwest National Laboratory (PNNL) to determine the frictional behavior of metals—like those used in fuel injectors—in the hydrogen environment of a hydrogen internal combustion engine or fuel cell. The friction and wear characteristics of metallic materials depend largely on surface oxide films. However, a hydrogen environment is chemically reducing, so the loss of the surface oxide by wear will result in bare surface contact and an increase in friction and wear. The Program is also working to reduce emissions through the development of advanced particulate filters.

A new project was initiated to identify materials requirements for the operating conditions in homogeneous charge compression-ignition (HCCI) engines and demonstrate the feasibility of the "materials by design" approach to developing advanced materials for the most critical engine components. Collaborations have already been established with two companies to work together on materials needs. Interaction with industrial partners throughout the project is expected to result in the rapid transfer of materials improvements to industry.

Collaboration and Cooperation

As with other programs under FreedomCAR, collaboration and cooperation across organizations is a critical part of the APM Program. Throughout the FreedomCAR Program, scientists at the national laboratories are collaborating with manufacturers to identify and refine the materials characteristics necessary for meeting system performance requirements. Researchers at Lawrence Livermore National Laboratory (LLNL) are working with Ford Motor Company and Oak Ridge National Laboratory (ORNL) to develop low-cost, rapid-response nitrogen oxides (NO_x) sensors that can be used in feedback control loops to monitor and minimize NO_x emissions from diesel engines. There is also cooperation among national laboratories to take advantage of the expertise of each facility. ORNL and Argonne National Laboratory, for example, are collaborating in the development of higher-strength NdFeB permanent magnets that will enable significant reductions in the size, weight, and cost of electric motors used in hybrid vehicles. In another project, ORNL is characterizing ~5-micron-thick polymer films that are being developed by Sandia National Laboratories (SNL). SNL is funded by the Power Electronics Program to develop smaller, higher-temperature dc bus capacitors. SNL is using the information provided by ORNL to optimize the properties of the films in order to minimize manufacturing defects during capacitor winding. These electric drive system projects in turn are

regularly reviewed by the EE Technical Team of the U.S. Council for Automotive Research to get feedback on research direction and progress.

In addition to participation by national laboratories and large industries, the FY 2005 APM Program included important R&D conducted by a small business. Industrial Ceramic Solutions, LLC (ICS), located in Oak Ridge, Tennessee, is developing a ceramic filter to reduce particulate emissions from diesel engines. As in the collaborative efforts of national laboratories with industry, researchers at ICS are working closely with representatives from DaimlerChrysler, Ford, General Motors, and ORNL to develop a filter that will meet the emissions targets of the program.

Contractor-industry collaboration

Technology	Industrial partner
Capacitors	✓ TPL, Inc.
	✓ Brady Corporation
	✓ Steiner Film, Inc.
	✓ AVX, Inc.
	✓ Custom Electronics
Magnets	✓ IAP, Inc.
	✓ Magnaquench, UG, Inc.
	✓ Ability Engineering Technology
	✓ Electron Energy Corporation
	✓ Bronson and Bratton, Inc.
Carbon foam heat sinks	✓ Ford Scientific Research Laboratory
	✓ DaimlerChysler
	✓ General Motors Corporation
	✓ Delphi
	✓ Visteon
Fuel injectors	✓ Siemens, USA
	✓ Siemens, AG
	✓ Navistar/International Harvester
	✓ Imagineering Finishing Technologies
NO_x sensors	✓ Ford
	✓ Cummins Engine Company
	✓ Detroit Diesel
	✓ Honeywell
	✓ DuPont
Particulate traps	✓ Ford-Jaguar
	✓ GE Locomotive
	✓ Ahlstrom Paper
	✓ Tennaco Automotive
	✓ Arvin Meritor

Accomplishments

FY 2005 featured significant advancements in the two newest materials program areas. The following section highlights some of these noteworthy accomplishments.

Hydrogen Compatibility of Materials

Materials used in fuel cells or in internal combustion engines powered by hydrogen operate in a different environment from materials employed in gasoline or diesel engines. Engine manufacturers need to know how constant exposure to hydrogen affects the properties and performance of materials used for engine components. The friction and wear characteristics of metallic materials depend largely on surface oxide films. However, since a hydrogen environment is chemically reducing, the loss of the surface oxide film by wear will result in bare surface contact and an increase in friction and wear.

An exploratory study began at PNNL in 2004 to determine the frictional behavior of metals such as those used in fuel injectors in the environment of a hydrogen engine or fuel cell. The purpose is to understand and quantify the mechanisms that determine the friction coefficient and surface properties of materials in a 100% hydrogen service environment by comparing materials as received from the manufacturer with hydrogen-exposed samples. During FY 2005, PNNL and ORNL tested metallic injector materials used by Westport Innovations, a maker of fuel injectors. A high-pressure hydrogen test vessel was designed and built and used to expose injector components and materials samples to hydrogen at various pressures and temperatures for 47 hours. Following the exposure period, the materials were analyzed using electron microscopy and nanoindentation and nanoscratch measurements.

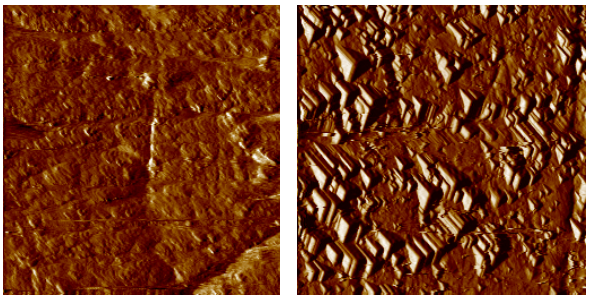

An injector material sample as-received (left) and after 47-h hydrogen exposure (right). Peak height maximum is 4–5 µm.

The analysis revealed material surface phenomena on the metal surfaces that appear to result from the formation of facets composed of a molybdenum/tungsten compound. The results showed that the friction coefficient of the materials increases with hydrogen exposure, largely as a result of the facet formation. Ongoing research will focus on evaluating new coatings, alloys, and piezo barrier materials under hydrogen explore and analyzing sliding and impact wear.

HCCI Materials

Interest in HCCI combustion has grown because of its potential to increase engine combustion efficiency and reduce emissions. However, HCCI will subject engine components to higher temperatures and pressures. Operating temperatures for diesel engines will exceed 1600°F, and pressures may exceed 2000 psi, approximately four times the pressure in a conventional combustion engine. Such severe operating conditions will require much improved materials performance to take advantage of the HCCI engine concept. The APM Program has initiated an effort to identify materials requirements for HCCI engines in automotive and truck applications and develop advanced, cost-effective materials through computational design.

The work is based on "materials by design," a concept and collection of materials R&D techniques involving modeling, correlation, and materials modification. Materials by design is ideally suited to cast and heavily thermally processed materials such as stainless steels, nickel alloys, cast irons, alloy steels, and brazed wrought aluminum alloys.

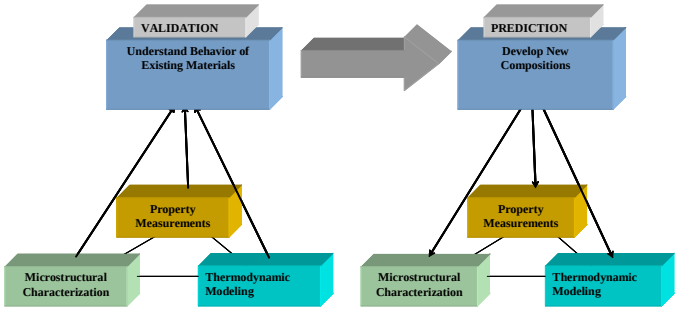

Overall approach for materials by design.

The initial task is to identify critical materials requirements for HCCI engines based on operating conditions. This task will include interaction with several advanced engine/component design companies. The outcome of this task will be ranking the highest-priority items for study with materials by design. Task 2 is to demonstrate the feasibility of materials by design for the highest-priority item, and task 3 is to use modeling and experimental validation to improve the materials performance.

Discussions with automotive and truck companies in 2005 identified four materials needs to support advanced engine concepts such as HCCI: aluminum for charge air coolers, cast iron for exhaust manifolds, nickel alloys for exhaust valves, and alloy steels for fuel injectors. Collaborations were established with two companies to work together on materials needs.

As a first step in materials development through computational design, phase equilibrium calculations were conducted on three published nickel-based alloy compositions. The weight percent of γ' showed a qualitative agreement with published fatigue data for two of three alloys used. Ongoing work will quantify the correlation between fatigue properties and phase type and will validate weight percent on experimental-size heats of selected compositions.

Future Direction

The APM Program will continue to work closely with FreedomCAR partners and industry to understand requirements related to propulsion materials. Building upon the recent advances in materials technologies, many of this year's projects will be moved out of the laboratory and over to industry for testing. For example, ICS will work with identified strategic manufacturing partners in the automotive industry to move the durability and soot-holding capacity performance of the diesel particulate filter cartridge into compliance with the system requirements of automotive original equipment manufacturers. LLNL, Ford, and ORNL have formed a partnership to develop and prototype a NO_x sensor and control system to control the operation of NO_x traps and engine emissions. Other projects will continue to refine manufacturing requirements and necessary characteristics to meet the challenges of the FreedomCAR program.

As advanced automotive technology developments uncover new challenges, the APM Program will continue to provide breakthrough technology solutions through collaboration with industry, FreedomCAR partners, national laboratories, and small businesses.

Project Abstracts

The remainder of this report communicates the progress achieved during FY 2005 under the APM Program. It consists of nine abstracts of national laboratory projects—four that address power electronics and five that address combustion and emission technologies. The abstracts provide an overview of the critical work being conducted to improve these systems, reduce overall cost, and maintain component performance. In addition, they provide insight into the challenges and opportunities associated with advanced materials for high-efficiency automobiles.

Rogelio Sullivan

Team Leader, Materials Technologies
Office of FreedomCAR and Vehicle Technologies
Energy Efficiency and Renewable Energy

2. POWER ELECTRONICS

A. Low-Cost, High-Energy-Product Permanent Magnets

Y. S. Cha and John R. Hull
Energy Technology Division, Bldg. 335
Argonne National Laboratory, Argonne, IL 60439
(630) 252-5899; fax: (630) 252-5568; e-mail: yscha@anl.gov

DOE Materials Technologies Team Leader: Rogelio Sullivan
(202) 586-8042; fax: (202) 586-1600; e-mail: rogelio.sullivan@ee.doe.gov
ORNL Technical Advisor: David Stinton
(865) 574-4556; fax: (865) 241-0411; e-mail: stintondp@ornl.gov

Contractor: Argonne National Laboratory, Argonne, Illinois
Prime Contract No.: W-31-109-Eng-38

Objective

- Develop a low-cost process to fabricate anisotropic NdFeB permanent magnets (PMs) with an increase of up to 25% in energy product to enable significant size and weight reductions in traction motors for hybrid vehicles.

Approach

- Use high fields of superconducting solenoids to improve magnetic grain alignment while pressing compacts for sintering, thus producing higher-performance magnets.
- Develop an automated press system, including the superconducting magnet, for the fabrication of NdFeB PMs.
- Conduct an economic analysis of the automated superconducting PM fabrication system and compare it with the conventional system.

Accomplishments

- Designed and fabricated a new tapered die and punch set to avoid the cracking problem during compact ejection from the die.
- Fabricated near-final-shape powdered compacts under various alignment fields using the modified and the new die and punch sets to demonstrate that compacts can be fabricated at much faster rates, which is essential for the low-cost production of the permanent magnets.

Future Direction

- Conclude the project and prepare a final report that will include all the data and information obtained from the entire duration of the project.

Introduction

The strength of sintered NdFeB magnets greatly depends on the method by which the compact is magnetically aligned and pressed. Large blocks can be made by cold-isostatic pressing that are within 5% of their theoretical maximum; but these must be sliced, diced, and ground to final shape, making the

magnets very expensive. Magnets that are axial-die-pressed and sintered to near-final shape are the least expensive to make, but they have magnetic properties farthest from their theoretical maximums. The current industry goal is to fabricate higher-energy-product magnets by near-net-shape processing to avoid expensive machining operations. The major objectives of this project are to increase the energy product of the sintered PMs by 10 to 15% (to within ~10% of the theoretical maximum) and to develop low-cost methods of production for high-energy-product, near-final-shape PMs. The higher-performance magnets will replace ones made by traditional powder metallurgy processing and will enable significant size and weight reductions in traction motors for hybrid vehicles.

Approach

Our approach is to align the NdFeB powder in a superconducting magnet, which can generate magnetic fields much higher than those generated by the electromagnets presently used in industry. Alignment of the powder in these higher magnetic fields improves the properties of the PMs. To develop a low-cost mass-production method for high-energy-product PMs, we plan to design, fabricate, and demonstrate a semi-automated axial-die-press system for making near-final-shape NdFeB PMs.

Previously, a 9-T superconducting solenoid was procured and made operational. Production-grade magnet powder was obtained from Magnequench UG. The 3- to 5-micron single-crystal grains of powder were aligned and compacted at Argonne National Laboratory (ANL). Then the anisotropic compacts, with their grains mechanically locked in place, were returned to Magnequench UG for sintering, annealing, machining, and measuring of engineering magnetic properties.

Previously, we demonstrated that significant improvement of energy product (10–15%) can be achieved by using higher alignment fields (>2 T).[1] It was also demonstrated that near-net-shape PMs (with a diameter-to-length ratio as low as 0.25) can be fabricated using the present technology. Industry considers an improvement in energy product of as little as 3–5% over current PMs to be significant. The progress achieved so far is based on a batch process at ANL. Major issues remaining for acceptance of the technology by industry are (1) to demonstrate that PMs can be made at a much faster rate than in the batch process, and (2) to demonstrate that the superconducting magnet and its associated press systems are economically feasible by conducting an economic analysis.

Results

In previous investigations, we encountered the problem that air is not being released fast enough during compact pressing, which may have caused the compact to crack during ejection from the die. To avoid this problem, the rate of pressure increase during compact pressing was kept quite slow. In order to make the production cost lower, the present process must be improved and the rate of pressing must be increased significantly. In FY 2005, we modified the existing 5/8-in. die and punch set to alleviate the trapped air problem during compact pressing. We worked with engineers and designers at Bronson and Bratton, Inc. (a powder metallurgy tooling company located in a suburb of Chicago) on the design of the die and punch system. To allow air to escape more easily during compact pressing, it was decided to cut six flats (0.192 in. wide and 60° apart) along the axial direction of the punch and a 0.20-in.-wide circular groove near the face of the punch. A contract was issued to Bronson and Bratton to modify the existing 5/8-in. die and punch system. A photograph of the finished punches is shown in Figure 1. This design will reduce the resistance to air flow and still maintain relatively tight clearance between the die and punch during compact pressing. After the punches were delivered, we fabricated 10 compacts using the new punches, all at a magnetic field of 2 Tesla, to determine if there is any improvement in processing the compacts. We observed that the pressurization rate of the compact can be increased significantly over that of previous compacts made by using the original punches. We also noticed that pressure fluctuations were reduced during the early stage of the pressing. These observations clearly indicate qualitatively that air was able to escape faster and easier from the die because the resistance to air flow was reduced. Another indication that the modified die and punch set reduces hydraulic resistance came during powder filling of the die under gravity. After the die was filled with an appropriate amount of powder, it was observed that the top punch fell to its final position

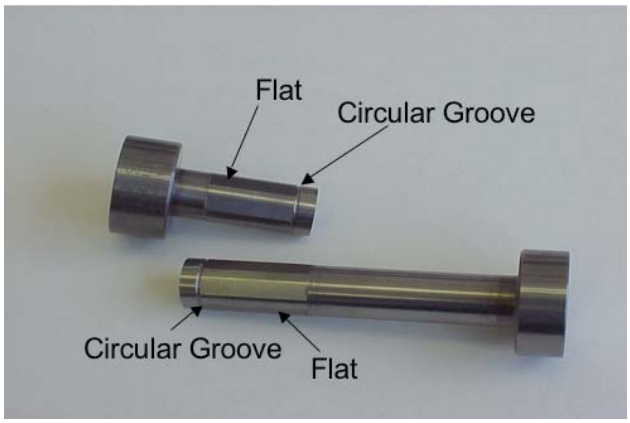

Figure 1. Photograph of the punches modified to alleviate the trapped air problem.

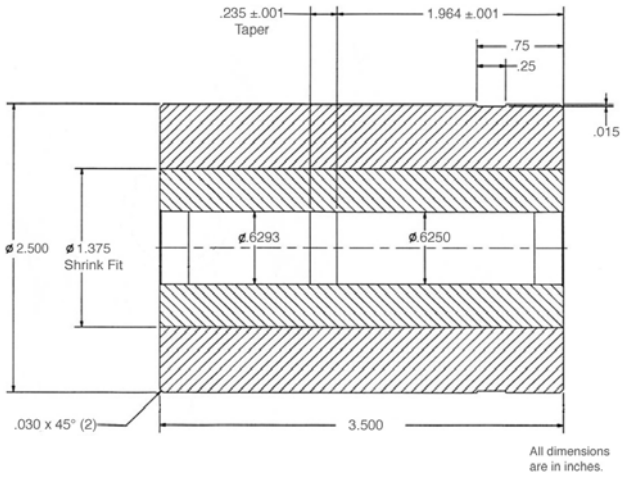

Figure 2. Schematic diagram and dimensions of the tapered die.

in about 15 seconds, compared with 3 minutes when the old die and punch set was used.

In the past, powdered compacts frequently cracked during ejection from the die. To improve the success rate of compact ejection, a new die and punch set was designed in collaboration with Bronson and Bratton. The die is tapered slightly as shown in Figure 2. The thickness of the compact is 0.235 in. (5.969 mm), and the diameter changes from 0.6250 to 0.6293 in. (15.875 to 15.984 mm) over the thickness of the compact. These dimensions are based on previous experience that the average diameter of the compact increased from 0.625 to 0.6290 in. (15.875 to 15.977 mm) during ejection from the die. The slightly tapered design is supposed to reduce the friction during compact ejection, which may alleviate the cracking problem encountered previously. Following the completion of the design, a purchase order was issued to fabricate the tapered die and punch set. We received the new die and punch set at the end of March of 2005. We restarted the superconducting magnet and fabricated about a dozen compacts under different magnetic fields. We had 100% success, and not a single compact cracked during and after ejection from the die. The results are very encouraging. In addition to alleviating the cracking problem using this tapered die and punch set, we were able to further increase the rate of pressurization during compact pressing without causing cracks in the ejected compact.

Last year, we contracted with Data Decisions to conduct an economic study of the superconducting PM manufacturing system, which was recommended after the 2003 DOE review meeting. The main objective is to compare the cost of manufacturing PMs using the superconducting technology and the cost with conventional technology using electromagnets. A preliminary report was received. Review comments were received from DOE, ANL, and Oak Ridge National Laboratory. These comments were transmitted to Data Decisions and a revised report was received. A major conclusion of the economic study is that the capital cost of the superconducting PM fabricating system is about the same as for a conventional system, while the energy product of magnets products by the superconducting system is approximately 15% higher than in magnets produced by a conventional system. The report is being finalized and will be issued in the near future.

Conclusions

Previously, we demonstrated that significant improvement of energy product (10–15%) can be achieved by using higher alignment fields (>2 T). Industry considers an improvement of 3–5% in the energy product of current PMs to be significant. It was also demonstrated that near-final-shape PMs (with a diameter-to-length ratio as low as to 0.25) can be fabricated with this new technology. Major issues remaining for acceptance of the technology by industry are (1) to demonstrate that PMs can be made at a much faster rate than in the batch process and (2) to demonstrate that the superconducting PM fabrication technology can be cost-effective by conducting an economic analysis. In FY 2005, we modified the existing 5/8-in. die and punch set to alleviate the trapped air problem during compact pressing. We also designed and fabricated (in

collaboration with Bronson and Bratton) a tapered die and punch set to avoid compact cracking during ejection from the die. We fabricated a total of 24 compacts under different alignment fields using the modified and the new tapered die and punch sets. The results are very encouraging. By using the tapered die and punch set, we were able to eliminate the compact cracking problem during ejection from the die. Furthermore, we were able to increase significantly the rate of pressurization during compact pressing. Both of these results demonstrate that the PMs can be fabricated at much faster rate than with the batch process employed before. This is essential for the low-cost production of PMs using the superconducting technology.

In FY 2005, we reviewed and revised the report on the economic analysis of the superconducting PM manufacturing technology. It was concluded that the capital cost of the superconducting PM fabricating system is about the same as for a conventional system, while the energy product obtained using the former is approximately 15% higher than that obtained with the latter.

In FY 2006, we plan to have an orderly close-out of the project by preparing a final technical report, which will include all the results and accomplishments from the inception of the project.

References

1. *2003 Annual Progress Report, Automotive Propulsion Materials*, U.S. Department of Energy, Office of Energy Efficiency and Renewable Energy, Office of FreedomCar and Vehicle Technologies, Washington, D.C.

Publications/Presentations

Y. S. Cha and J. R. Hull, "Low-Cost High-Energy-Product Permanent Magnets," presented at the Annual Review of Advanced Power Electronics and Electrical Machines, DOE FreedomCAR and Vehicle Technologies Program, May 3–5, 2005, Oak Ridge, TN.

R. E. Wolf, An Economic Study of the Manufacture of High Energy Permanent Magnets for Traction Motors in Hybrid Electric Vehicles, submitted by Data Decisions to Argonne National Laboratory, revised April 2005.

B. Characterization of Rare Earth Permanent Magnets for Automotive Applications

Edgar Lara-Curzio, Andrew Payzant, and Chris Cofer
Building 4515, MS-6069
Oak Ridge National Laboratory
(865) 574-1749; fax: (865) 574-6098; e-mail: laracurzioe@ornl.gov

DOE Materials Technologies Team Leader: Rogelio Sullivan
(202) 586-3976; fax: (202) 586-9811; e-mail: rogelio.sullivan@ee.doe.gov
ORNL Technical Advisor: David Stinton
(865) 574-4556; fax: (865) 241-0411; e-mail: stintondp@ornl.gov

Contractor: Oak Ridge National Laboratory
Prime Contract No.: DE-AC05-00OR22725

Objective

- Determine the effect of thermal cycling on the magnetic and mechanical properties of sintered and bonded rare earth permanent magnets.

Approach

- Develop a test facility with an environmental chamber capable of cycling temperature between –40 and 300°C.
- Develop instrumentation to determine in real time the magnetic strength of test specimens as a function of temperature and number of thermal cycles.
- Evaluate the residual mechanical properties of sintered and bonded rare earth permanent magnets after thermal cycling.

Accomplishments

- Developed a test facility capable of cycling temperature between –40 and 300°C. The test facility is instrumented to determine, in real time, the magnetic strength of sintered and bonded rare earth permanent magnets.
- Determined that the magnetic strengths of bonded and sintered permanent NdFeB magnets decrease linearly with temperature and, at a given temperature, decrease exponentially with the number of thermal cycles.

Future Direction

- The project was completed at the end of FY 2005.

Introduction

Achieving FreedomCAR and Fuel Partnership goals will require the development of new technologies for electric machinery. The new technologies must be compatible with high-volume manufacturing; must ensure high reliability, efficiency, and ruggedness; and must simultaneously reduce cost, weight, and volume. Key components for hybrid vehicles include motors, sensors, and control systems.[1]

While permanent magnet motors have the highest power density, they don't have a sufficient constant power speed range; and their cost is too high because of the costs of magnet materials,

magnet manufacturing, and rotor fabrication. Sintered and polymer-bonded particulate magnets are being developed with the objectives of increasing their useful operating temperature to 150°C and decreasing the cost to about 25% of the current price of approximately $90/kg. Furthermore, these magnets should be rugged and reliable enough to operate in harsh environments—including extreme temperatures, humidity, and thermal cycling—for 150,000 miles or 15 years. The objective of this project is to determine the resistance of sintered and bonded NeFeB permanent magnets to thermal cycling between –40 and 150°C.[1]

Approach

In FY 2004, a test facility was designed and constructed to evaluate the resistance of sintered and bonded rare earth permanent magnets to thermal cycling. The test facility consists of a chamber capable of cycling temperature between –40 and 300°C. Temperatures below ambient temperature are achieved by dispersing liquid nitrogen into the chamber using compressed air and a solenoid valve, while heating is achieved using compressed air and a set of cartridge heaters. The interior of the chamber, which has dimensions of 61 × 30 × 30 cm, is lined with one layer of insulating material. Temperature measurements are obtained with type K thermocouples. By placing thermocouples at various locations it was demonstrated that the temperature was uniform within 3°C anywhere within the chamber.

A computer-based system was assembled for controlling the operation of the test facility and for data acquisition. The system consists of a personal computer, a high-speed A/D data acquisition card, a customized computer application using the commercially available package LabView, and a digital temperature controller. Figure 1 depicts the experimental setup developed for this project.

Magnetic Properties

Changes in magnetic properties were determined as a function of temperature and number of thermal cycles by measuring the voltage induced when the magnets under evaluation move through a coil at a given temperature and after a predetermined number of thermal cycles.

Figure 1. Experimental setup for the project.

The permanent magnets under evaluation, which were shaped in the form of prismatic beams, were bonded at various locations along 6.5-mm-diameter stainless steel rods. A set of 16 rods was attached to a frame that was coupled to a pneumatic actuator. Figure 2 depicts the array of 16 stainless steel rods and their position within the chamber. The reciprocating motion of the pneumatic actuator resulted in the motion of the permanent magnets through coils, which are placed around plastic tubes that are concentric to the rods (Figure 3). The motion of the magnets through the coils induces a voltage in the coils. According to Faraday's law,[2] the voltage induced in the coil will be proportional to the change in the magnetic flux through the coil (Φ), according to

$$V = -\frac{d\Phi}{dt} \ , \qquad (1)$$

where the magnetic flux through the coil is given by

$$\Phi(t) = B(t)\, N\, A \ . \qquad (2)$$

B(t) is the magnetic field of the magnet, *N* is the number of turns in the coil, and *A* is the cross-sectional area of the coil.

The voltage induced across the terminals of the coil is recorded as a function of temperature and as a function of the number of thermal cycles. Figure 4 shows a voltage trace resulting from the displacement of a bonded permanent NdFeB magnet through one of the coils.

Figure 2. Array of 16 stainless steel rods within the chamber.

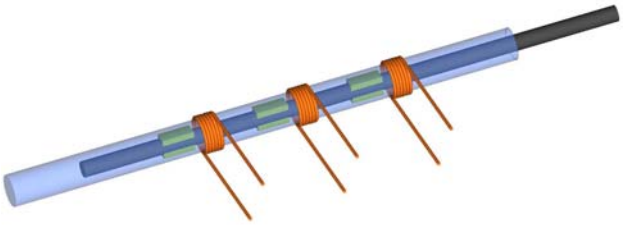

Figure 3. Stainless steel rods, with magnets attached, move through coils placed around plastic tubes that surround the rods.

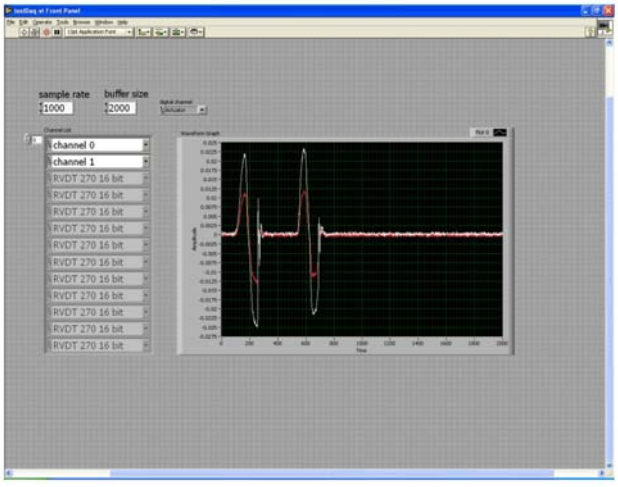

Figure 4. Voltage trace resulting from the movement of a magnet through a coil

Materials

Bonded and sintered permanent NdFeB magnets were used in this investigation. Test specimens shaped in the form of prismatic beams 2.0 × 1.5 × 26.0 mm were obtained from larger pieces by diamond grinding. In the case of bonded magnets, they were obtained from cylindrically shaped test specimens that had been processed by dynamic magnetic compaction. To reduce stress concentrations for subsequent mechanical testing, the test specimens were chamfered at the corners. Figure 5 is a picture of bonded NdFeB test specimens along one of the cylindrical magnets processed by dynamic magnetic compaction.

Figure 5. Test specimens along a cylindrical magnet processed by dynamic magnetic compaction.

Experimental

Test specimens were subjected to the temperature schedule shown in Figure 6. The temperature of the test chamber was increased/ decreased at a constant rate of 10°C/min. After reaching a set point (– 40°, 0°, 50°, 100° and 150°C), the chamber was allowed to reach thermal equilibrium in 15 minutes. Then the pneumatic actuator was operated and the voltages induced by the motion of the test specimens through their corresponding coil were recorded. After a prescribed number of thermal cycles, a set of test specimens was removed from the chamber and their flexural strength was determined at ambient conditions.

Results

Figure 7 shows the magnitude of the voltage recorded for a sintered NdFeB permanent magnet as a function of temperature and number of thermal cycles. It was found that the magnitude of the voltage decreased both with temperature and with number of thermal cycles. Figure 8 shows the temperature dependence of the voltage recorded after different numbers of cycles. It was found that the magnitude of the voltage decreased linearly with temperature, whereas for a given temperature, the

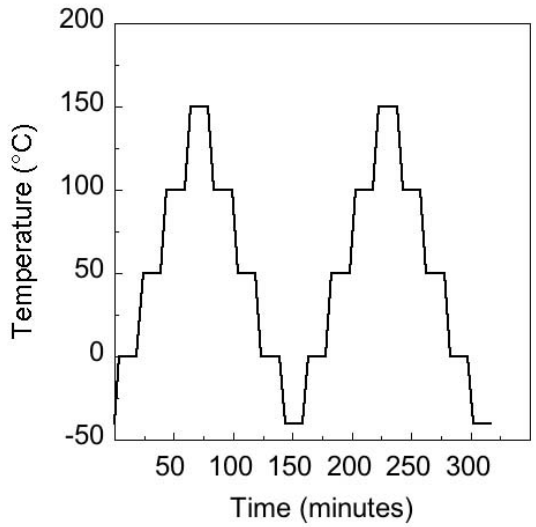

Figure 6. Temperature schedule to which magnet specimens were subjected.

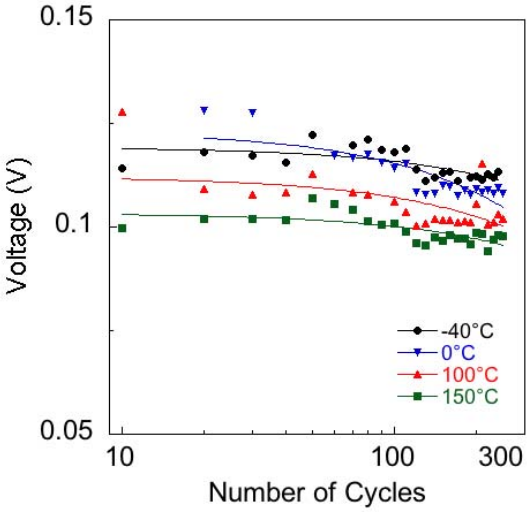

Figure 7. Voltage recorded for sintered permanent magnet as a function of temperature and number of thermal cycles.

voltage decreased with number of thermal cycles according to the following equation:

$$V=Voe^{-kN} \quad , \qquad (3)$$

where *Vo* and *k* are constants and *N* is the number of thermal cycles. Because the magnitude of the voltage is directly proportional to the strength of the magnetic field induced by the magnet, then it can be concluded that the strength of the magnetic field of

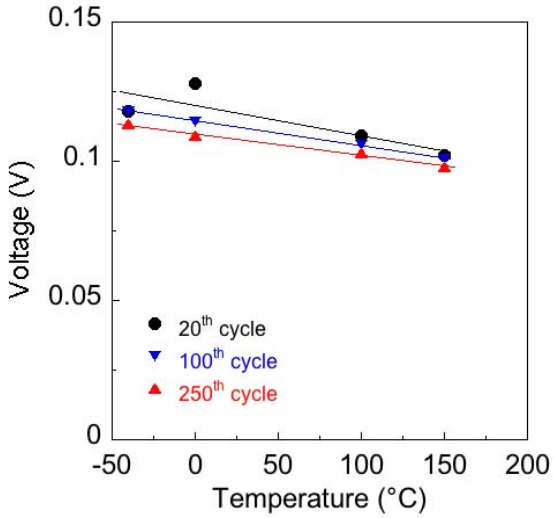

Figure 8. Temperature dependence of voltage recorded after various numbers of cycles.

NdFeB decreased with temperature and with the number of thermal cycles between –40° and 150°C.

The flexural strength of bonded and sintered NdFeB permanent magnets was determined in 4-point bending according to ASTM standard test method C1161. The flexural strength was calculated according to the following relationship:

$$\sigma_{flexural} = \frac{3PL}{4bd^2} \quad , \qquad (4)$$

where *P* is the peal load, *L* is the support span (20.52 mm), and *b* and *d* are the width and thickness, respectively, of the test specimen. The flexural strength values were corrected for the chamfered corners.

Figure 9 shows a plot with the results from the flexural evaluation of bonded and sintered NdFeB permanent magnets. It was found that sintered NdFeB permanent magnets were stronger than bonded NdFeB permanent magnets by almost one order of magnitude and that their flexural strength decreased with the number of thermal cycles according to the following equation:

$$\sigma=\sigma_o N^{-a} \quad , \qquad (5)$$

where σ_o and *a* are constants. It was found that after 250 cycles, *a*=0.02 for sintered NdFeB magnets while *a*=0.03 for bonded NdFeB magnets.

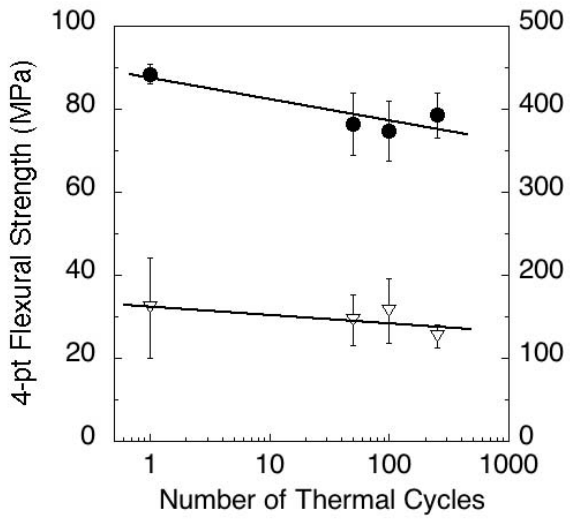

Figure 9. Results of flexural evaluation of bonded and sintered permanent magnets.

The fracture surfaces of a selected number of test specimens were examined by scanning electron microscopy to identify strength-limiting flaws and microstructural changes, if any, that might have been induced by thermal cycling. Figure 10 shows a scanning electron micrograph of the fracture surface of a sintered magnet after 100 thermal cycles. It was found that, in most cases, failure originated at locations of non-uniform microstructure.

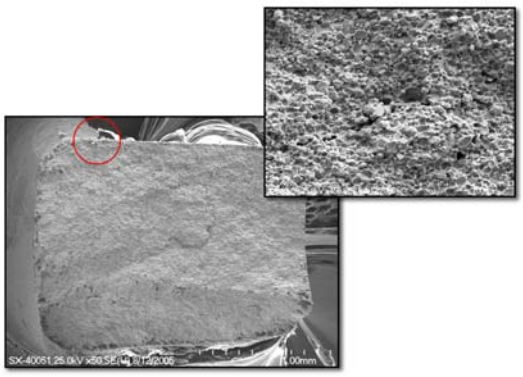

Figure 10. Scanning electron micrograph of the fracture surface of a sintered magnet after 100 thermal cycles.

Summary

A test facility was designed and fabricated to evaluate the effect of thermal cycling on the magnetic and mechanical properties of sintered and bonded PMs. The test facility is capable of operating between –40 and 300°C and of providing real-time measurement of the magnetic strength of test specimens. It was found that the magnetic strength of bonded and sintered permanent NdFeB decreases linearly with temperature and that at a given temperature, it decreases exponentially with the number of thermal cycles. It was also found that sintered NdFeB magnets were 10 times stronger than bonded NdFeB magnets and that the flexural strength of both decreased with the number of thermal cycles.

References

1. *2002 Annual Progress Report, Automotive Propulsion Materials*, U.S. Department of Energy, Office of Energy Efficiency and Renewable Energy, Office of FreedomCar and Vehicle Technologies, Washington, D.C.
2. J.D. Jackson, *Classical Electrodynamics*, John Wiley and Sons, New York, 1967.

C. Carbon Foam for Cooling Power Electronics

Nidia C. Gallego
Oak Ridge National Laboratory
P.O. Box 2008, MS 6087, Bldg. 4508
Oak Ridge, TN 37831-6087
(865) 241-9459; fax: (865) 576-8424; e-mail: gallegonc@ornl.gov

Albert Shih, Steve White
S. M. Wu Manufacturing Research Center
University of Michigan

Anthony G. Straatman
Department of Mechanical and Materials Engineering
University of Western Ontario
London, Canada

Brian E. Thompson and Qijun Yu
Foam Application Technologies Inc.
Mayaguez, Puerto Rico

DOE Materials Technologies Team Leader: Rogelio Sullivan
(202) 586-8042; fax: (202) 586-1600; e-mail: rogelio.sullivan@ee.doe.gov
ORNL Technical Advisor: David P. Stinton
(865) 574-4556; fax: (865) 241-0411; e-mail: stintondp@ornl.gov

---

Contractor: Oak Ridge National Laboratory, Oak Ridge, Tennessee
Prime Contract No.: DE-AC05-00OR22725

Objectives

- Collaborate with an automotive partner to develop a carbon foam heat exchanger and heat sink designs that dissipate more than 30 W/cm^2 using standard cooling fluids.
- Develop and demonstrate designs for reducing weight and enhancing heat transfer in power electronic thermal management systems using high-thermal-conductivity carbon foam.
- Determine the foam structure or morphology that results in optimum heat transfer for various thermal management applications.

Approach

- Study fundamental mechanisms of heat transfer in carbon foam and develop an engineering model that allows comparison of conventional and carbon foam heat exchangers.
- Redesign and build a test apparatus for measuring the heat transfer coefficients and pressure drops of heat sinks made of carbon foam.
- Design and build a thermosyphon test rig to study the performance of carbon foams in this system.

Accomplishments

- Formed a team consisting of Oak Ridge National Laboratory (ORNL), the University of Western Ontario, and Ford Motor Company to develop a test setup for evaluating the performance of carbon foam heat sinks.
- Produced foams with a variety of pore structures; measured the heat transfer and pressure drop obtained by passing water through the foam samples.
- Demonstrated the capability of a graphite foam–based thermosyphon to cool 65 W/cm^2 at a temperature of 56°C.
- Developed an engineering model for use in the development of electronic heat sinks.

Future Direction

- Modify designs of foam-based heat exchangers based on new foam properties.
- Determine whether the foam's increased surface area or internal volume assists the most in boiling heat transfer.
- Develop a design for a carbon foam-based heat sink for use in automotive power electronics.

Introduction

Porous carbon foam developed at ORNL[1,2] is being investigated as a material to improve both single-phase and multiphase heat transfer. Carbon foam has a high effective conductivity (40–160 W/m K)[2] because of the high material conductivity of the graphitized carbon material (800–1900 W/m K). In comparison, similar porous aluminum foams have effective conductivities of 2–26 W/m K, resulting from material conductivities of only 140–237 W/m K (for various aluminum alloys).[3] The high effective conductivity of the porous carbon foam combined with the open, interconnected pore structure is conducive to high internal heat transfer and the potential for high convective heat transfer enhancements.

This year's work focused on the characterization of the hydrodynamic and thermodynamic performance of the foam and how it impacts the development of modern heat exchangers and electronic heat sinks. A combination of experiments and modeling is being conducted to explore the use of porous carbon foam in the removal of heat from power electronics.

Additionally, a thermosyphon test rig was designed and built for the evaluation of the performance of carbon foam in these types of cooling systems.

Experimental Study

Experiments are being conducted on a small-scale test rig to measure the heat transfer and pressure drop across blocks of porous carbon foam. The test setup shown in Figure 1 consists of a channel with a fluid inlet and outlet, a heating element, and instrumentation to measure the flow rate, the heat input, and the fluid pressure drop across the foam block (from position 1 to 2). Porous carbon foam blocks of different porosities and pore diameters were subjected to a range of flow rates and power densities to quantify variations in pressure drop and thermal effectiveness in the foam structure (characterized by porosity, ε, and void diameter, D_p) and the flow Reynolds number (defined as $\mathrm{Re}= \rho V_{pb} D_{ep}/\mu$, where ρ is the density of the fluid, V_{pb} is the channel bulk velocity, D_{ep} is the equivalent solid particle diameter of the foam and μ is the dynamic viscosity of the fluid).

For all specimens tested, the fluid pressure-drop was observed to vary linearly with *Re* for low Reynolds numbers, followed by a parabolic variation for higher Reynolds numbers. Figure 2

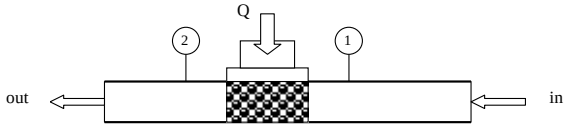

Figure 1. Schematic of experimental setup showing the position of the carbon foam, the fluid inlet (in) and outlet (out), and the heat input (Q).

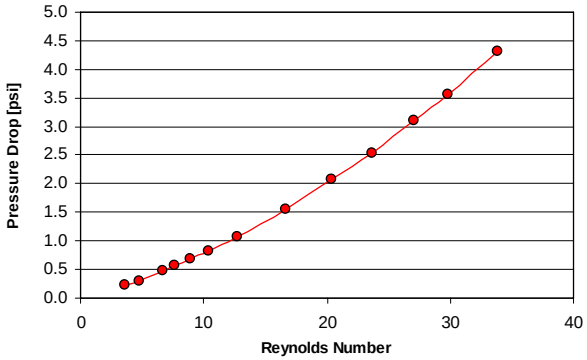

Figure 2. Variation of pressure-drop with Reynolds number for a specimen of porous carbon foam of porosity 0.88 and pore diameter 400 μm.

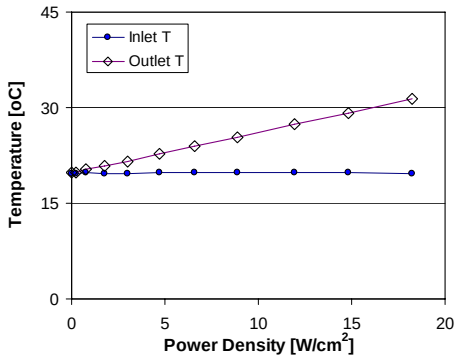

Figure 3. Variation of temperature rise (outlet – inlet) with power density at a Reynolds number of *Re*= 13 for a specimen of porous carbon foam of porosity 0.88 and pore diameter 400 μm.

shows the pressure drop as a function of Reynolds number for a foam specimen of porosity 0.88 and pore diameter 400 μm. The pressure data are used to obtain permeability and form drag coefficients based on the classical Darcy-Forchheimer law for porous media. The permeability of the foam is seen to be a strong function of both porosity and pore diameter, as might be expected, but it is also seen to be dependent on the structure of the cell windows connecting the cells. The permeability is considerably lower than the ideal permeability predicted by the unit-cube model of Yu et al.[4] and the permeability of aluminum foams.

The thermal performance of the foam specimens was determined based on the temperature rise of the fluid across the specimen and by a thermal model that considers the block to be an extended surface heated from one side. Figure 3 shows variations of the inlet and outlet water temperatures over a range of power densities for a Reynolds number *Re*= 13. The thermal performance is observed to be considerably better than that of an equivalent aluminum (or other metal foam) block owing to the higher effective conductivity and the increased surface-area-to-volume ratio of the porous carbon foam.

Modeling Study

For the modeling work, the cylindrical cavity-style heat sink shown in Figure 4 was considered. The heat sink is attached to a metal substrate, which is then pressed firmly against the electronic component. The resistant analog for the heat sink

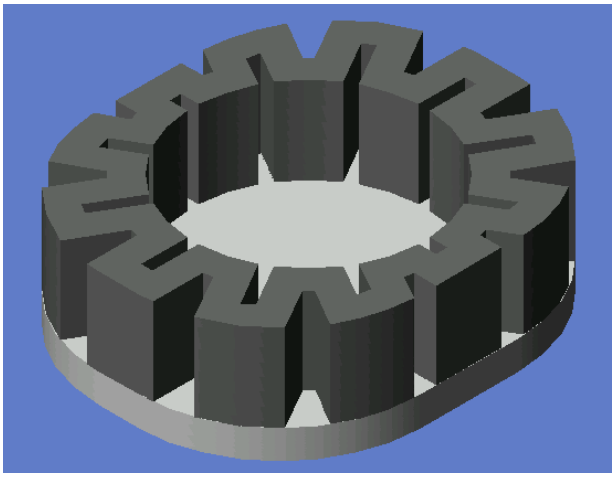

Figure 4. CAD image of a cylindrical-shaped electronic heat sink.

shown in Figure 4 is given in Figure 5. Expressions for the resistances in the thermal circuit were derived using the unit-cube model of Yu et al.[4] and established expressions for the Nusselt number modified to be suitable for porous carbon foam.

Thermal Resistances

R1: Bond contact thermal resistance between the integrated heat spreader (IHS) of the processor and the heat spreader (HS) of the heat sink

R2: Conduction thermal resistance through the HS of the heat sink

R3: Bond contact resistance between the HS and the carbon fin of the heat sink

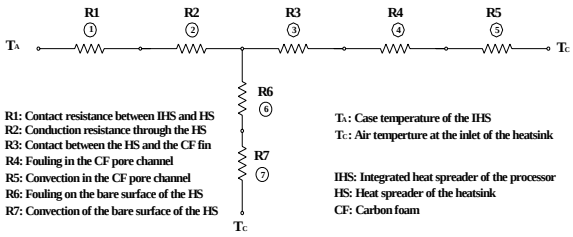

Figure 5. Electrical analog of thermal circuit for cylindrical heat sink.

R4: Fouling resistance in the pore channel of the carbon foam

R5: Convection thermal resistance in the pore channel of the carbon foam fin

R6: Fouling on the bare surface of the HS at the carbon foam fin root

R7: Convection thermal resistance on the bare surface of the HS at the carbon foam fin root

Air Pressure Loss

$$\Delta P_a = \left(\frac{\mu_a}{K} V_{pba} + \frac{c_f}{\sqrt{K}} \rho_a V_{pba}^2 \right) L_e , \qquad (1)$$

where μ_a and ρ_a are the air viscosity and density evaluated at the air average temperature. c_f is the Forchheimer coefficient of the carbon foam. L_e is the equivalent length of the pore channel, and is determined by

$$L_e = \left(\frac{1+\sqrt{2}}{2} \right) T_F \ . \qquad (2)$$

Sample Design of Carbon Foam Heat Sink with Aluminum Spreader

Carbon foam:

- ORNL 219 carbon foam with a permeability of 8.3781E-10 m^2 (equivalent of $f_{pb}=0.1$) and a Forchheimer coefficient of 0.0982
- Pore diameter D: 500 um
- Porosity ε: 90%
- Thermal conductivity of the solid phase k_s: 1500 W/m.K
- Density of the solid phase ρ_s: 2.15 g/cm^3

Heat sink configuration:

- Inside diameter of the carbon foam fin D_i: 50.8 mm (2 in.)
- Outside diameter of the carbon foam fin (average) D_o: 76.85 mm (3.0256 in.); $D_o=(a+b)/2$
- Long axis a: 83.2 mm (3.2756 in.)
- Short axis b: 70.5 mm (2.7756 in.)
- Thickness of the heat spreader t_{HS}: 6.35 mm (0.25 in.)
- Thermal conductivity of the heat spreader k_{HS}: 218 W/m.K
- Density of the heat spreader ρ_{HS}: 2.15 g/cm^3
- Thermal conductivity of the bonding material k_1 and k_3: 48 W/m.K
- Thickness of the bonding layer t_1 and t_3: 0.3969 mm (0.015625 in.)

Table 1 compares the size and volume of the heat sink made from a carbon foam fin attached to the aluminum heat spreader (Figure 4) with an equivalent-performance aluminum fin heat sink.

Thermosyphon System

A thermosyphon test rig was designed and built for the evaluation of carbon foams in this type of cooling system. A thermosyphon uses the latent heat of vaporization of a low-boiling-point fluid to dissipate heat. The heat is transferred from the source to the graphite foam, which is submerged in the fluid. The foam increases the surface area and nucleation sites for boiling to occur. The vapor formed rises into the condenser section of the system where it is condensed and drips back down to the evaporator section. This forms a closed-loop system that allows the heat to be transferred from a small source to a larger area where the condensing takes place.

In previous work, Coursey et al.[5] used a thermosyphon with carbon foam to study the effects of fluid level and type, and chamber pressure. Fluid level and type (FC-72 compared with FC-87) were both found to be insignificant as long as the fluid covered the entire piece of foam. Lower saturation pressures provided higher heat fluxes at lower wall temperatures. They cooled 50 W/cm^2 at a wall temperature of 85°C. Park, Kang, and Kim[6] also investigated fluid levels or charge ratios and determined them not to be significant. The limitations in heat transport were different for the

Table 1. Comparisons between the size and weight of the sample carbon foam heat sink and an aluminum-finned heat sink with equivalent performance

	Aluminum fin heat sink	Carbon foam fin heat sink	Reduction
Size: cm^3	108.63	128.94	38.20%
Weight: g	150.00	92.05	38.63%

different charge ratios. For low ratios, dry-out occurred, causing the temperature in the evaporator to increase from the bottom; while for higher charge ratios, flooding limitation caused the evaporator temperature to increase from the top. Klett and Trammell[7] constructed a thermosyphon to cool a silicon CMOS chip using carbon foam as the heat spreader and FC-72 as the working fluid. They report a maximum heat flux of 118 W/cm^2 at a superheat of 24°C for a block of foam, while a slotted piece of foam reached 149 W/cm^2 at a superheat of only 11°C.

A photo and a schematic of the thermosyphon system built for the current project are shown in Figures 6 and 7, respectively. A generic heat source was created by using a cartridge heater embedded in a copper rod that was insulated in a low-conductivity PTFE housing. The heat is transferred axially along the copper rod and monitored by measuring the temperature of the rod at three different locations. This allows for the heat flux to be calculated and the surface temperature of the rod to be extrapolated. The graphite foam is attached to the copper by first coating the bottom surface of the foam with copper and then soldering the two surfaces together.

The fluid used was HFE-7000, which is a 3m Novec Engineered Fluid that has a boiling point of 34°C. The fluid submerges the foam in a 5.08-cm-diameter and 5.08-cm-tall cylindrical Plexiglas housing. The vapor rises into a water-circulating copper coil condenser. The condenser flowed 21.5°C tap water at a rate of 7.57 L/h.

The thermosyphon was first tested without any foam attached to the copper. To show the temperatures reaching steady state, the system was degassed and then allowed to run at a setting of 55 V. The resulting temperature distribution over time is shown in Figure 8 for the three thermocouples located along the copper rod. Also the corresponding calculated heat flux is shown in Figure 9 as a function of time corresponding to the temperature difference between the middle and low thermocouples (q lm), the middle and high thermocouples (q mh), the low and high thermocouples (q lh), and the heat flux

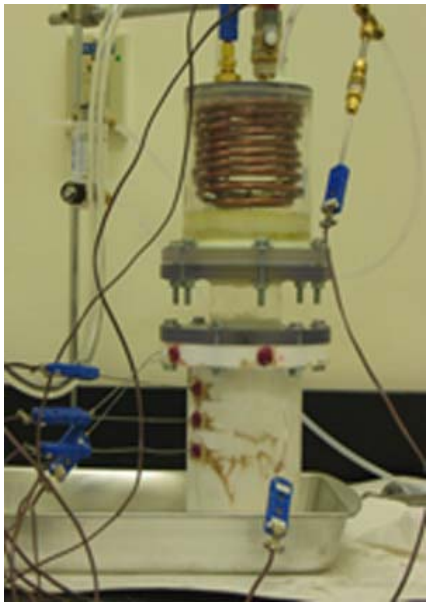

Figure 6. Picture of thermophyson test rig.

corresponding to the input voltage (q v). Both of the temperatures and heat fluxes reach a steady state setting in roughly 20 minutes from the start of recording. Typically the system takes a half hour to an hour to reach steady state, depending on the power increase. Only about 50% of the heat input into the system travels along the copper rod; the rest goes into heating the PTFE insulator.

The system was then run with and without using the degassing process, to show its importance. First there was a significant pressure buildup when no degassing occurred, which caused a loud hiss from the vapor escaping when the valve was opened. A properly degassed system exhibits lower wall temperatures at the same power input, as well as an increase in the critical heat flux, the transition from nucleate to film boiling.

The thermosyphon was tested with the graphite foam soldered to copper. The sample was 13.4 mm in diameter and 6.5 mm tall. The system was degassed and a sweep of input voltages was performed. The resulted boiling curve is shown in Figure 10. The heat flux was calculated using the measured temperature gradient, and the wall

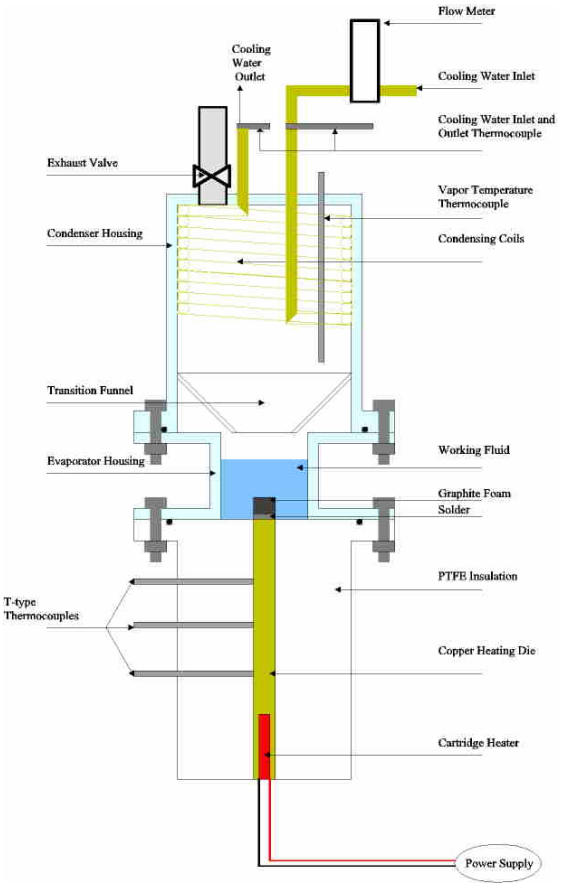

Figure 7. Schematic of thermophyson test rig.

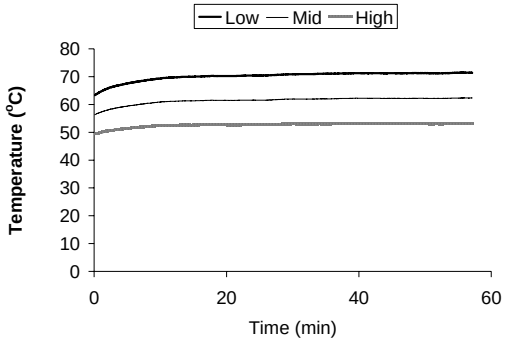

Figure 8. Temperature at three locations along the copper rod versus time for a voltage input of 55 V with bare copper rod exposed.

temperature was extrapolated using the heat flux and the temperature of the top thermocouple on the copper rod. The wall temperature represents the temperature of the copper rod just before the solder and does not account for variations in temperature across the solder. The maximum heat flux reached

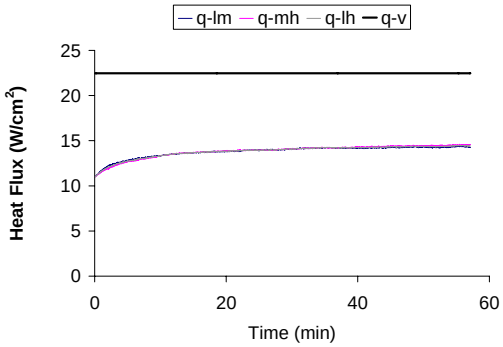

Figure 9. Heat input versus time for a voltage input of 55 V with bare copper exposed.

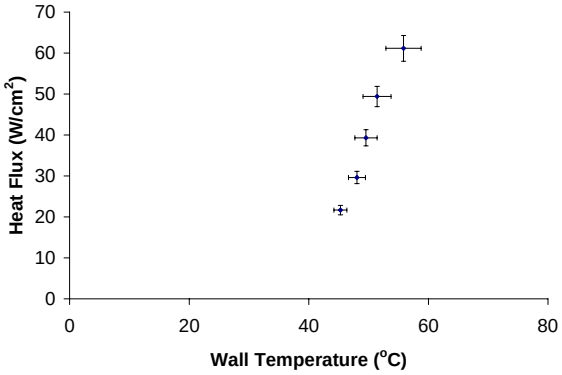

Figure 10. Boiling curve for foam sample of 13.4 mm diameter and 6.5 mm height..

for this sample was 61 W/cm^2 at a wall temperature of 56°C.

Next, the influence of foam dimensions, i.e. diameter and height, as well as the foaming pressure of the foam, will be investigated to optimize the parameters of the graphite foam used in the system.

Summary

Work in FY 2005 focused on characterizing the hydrodynamic and thermodynamic performance of carbon foam and its impact on the development of heat exchangers and electronic heat sinks. Experiments and simulations were conducted to explore the use of carbon foam to remove heat from power electronics, and a thermosyphon test rig was designed and built to evaluate its thermal performance.

A small-scale test rig measured heat transfer and variations in pressure drop across blocks of carbon foam of different porosities and pore diameters. For all specimens tested, the fluid pressure-drop

variation was linear with Reynolds number for low Reynolds numbers and parabolic for higher numbers. The thermal performance of carbon foam was observed to be considerably better than that of an equivalent aluminum (or other metal foam) block. The modeling study indicated that a carbon foam heat sink could be more than 38% smaller in size and weight than an aluminum finned heat sink of equivalent performance. The model also indicated that more porous carbon foams would be required to optimize the design of novel heat exchangers.

References

1. W.J. Klett, R. Hardy, E. Romine, C. Walls, T. Burchell, "High-Thermal-Conductivity, Mesophase-Pitch-Derived Carbon Foam: Effect of Precursor on Structure and Properties," *Carbon* **38**, 953–973 (2000).
2. N.C. Gallego and W.J. Klett, "Carbon Foams for Thermal Management," *Carbon* **41**, 1461–1466 (2003).
3. W.J. Paek, H.B. Kang, Y.S. Kim, and M.J. Hyum, "Effective Thermal Conductivity and Permeability of Aluminum Foam Materials," *Int. J. of Thermophysics*, 2**1**(2), 453–464 (2000).
4. Q. Yu, B.E. Thompson, and A.G. Straatman, "A Unit-Cube-Based Model for Heat Transfer and Pressure Drop in Porous Carbon Foam," submitted for publication to *ASME J. Heat Transfer*, 2004.
5. J.S. Coursey, H. Roh, K. Jungho, and P.J. Boudreaux, "Graphite Foam Thermosyphon Evaporator Performance Parametric Investigation of the Effects of Working Fluid, Liquid Level and Chamber Pressure," pp. 1–6 in *Proceedings of IMECE200*, November 2002.
6. Y.J. Park, H.K. Kang, and C.J. Kim, "Heat Transfer Characteristics of a Two-Phase Closed Thermosyphon to the Fill Charge Ratio," *International Journal of Heat and Mass Transfer* **45**, 4655–4661 (2002).
7. J.W. Klett and M. Trammell, "Parametric Investigation of a Graphite Foam Evaporator in a Thermosyphon with Fluorinert and a Silicon CMOS Chip," *IEEE Transactions on Device and Materials Reliability* **4**(3), 626–637 (September 2004).

Publications/Presentations

A.G. Straatman, N.C. Gallego, B.E. Thompson, H. Hangan, "Thermal Characterization of Porous Carbon Foam: Convection in Parallel Flow," *International Journal of Heat and Mass Transfer*, in press.

S.B. White, N.C. Gallego, D.D. Johnson; K.P. Pipe, A.J. Shih, and E. Jih, "Graphite Foam for Cooling of Automotive Power Electronics," pp. 61–65 in *IEEE Workshop on Power Electronics in Transportation*, 8th IEEE Workshop on Power Electronics in Transportation, October 2004.

D. Mechanical Characterization of Electronic Materials and Electronic Devices

A.A. Wereszczak, T.P. Kirkland, and H.-T. Lin
Ceramic Science and Technology Group
Oak Ridge National Laboratory
P.O. Box 2008, MS 6068, Bldg. 4515
Oak Ridge, TN 37831-6068
(865) 576-1169; fax: (865) 574-6098; e-mail: wereszczakaa@ornl.gov

DOE Materials Technologies Team Leader: Rogelio Sullivan
(202) 586-8042; fax: (202) 586-1600; e-mail: rogelio.sullivan@ee.doe.gov
ORNL Technical Advisor: David Stinton
(865) 574-4556; fax: (865) 241-0411; e-mail: stintondp@ornl.gov

Contractor: Oak Ridge National Laboratory, Oak Ridge, Tennessee
Prime Contract No.: DE-AC05-00OR22725

Objectives

- Mechanically characterize hydroxylated polystyrene (PVOH) dielectric films being developed by Sandia National Laboratories (SNL) for fabrication into higher-temperature, more compact dc bus capacitors.
- Quantify the mechanical performance of FY 2004 down-selected PVOH films as a function of temperature and link performances to allowable manufacturing and service conditions.

Approach

- Conduct tensile testing on SNL-supplied PVOH films and measure their strain-to-failure as a function of temperature.
- Using strain-to-failure, predict the minimum allowable radius of curvature that each film can withstand during processing into dc bus capacitors without failure.

Accomplishments

- Developed a bilaminate tensile test that enables both valid dielectric film mechanical characterization and ease of testing.
- Determined the average strain-to-failure of three PVOH films between room temperature and 140°C.
- Determined that one PVOH film (30 wt % 4010 Vectomer, no rubberizer, 40 wt % total solids, annealed at 225°C) consistently exhibited the largest strain-to-failure throughout the investigated temperature range.

Future Direction

- Develop a test method to enable quick evaluation of brittle-to-ductile temperature transition.
- Measure mechanical response of next-generation polymer dielectric films.

Introduction

A primary focus of the Power Electronics effort in the Automotive Propulsion Materials Program is to develop polymer capacitor technology that will replace current electrolytic, dc bus capacitors for power electronic modules in hybrid electric vehicles. The ultimate objective is to make the

power modules more compact while maintaining tight voltage and temperature requirements and long service life without compromise caused by mechanical breakdown of the dielectric film.

An anticipated capacitor geometry containing these dielectric films is a cylindrical one. The dielectric films would be subjected to rolling or mandrel wrapping during capacitor manufacture. If the films cannot mechanically withstand those bending actions, they will fail or fracture, rendering the capacitor inoperable. Therefore, it is desirable to identify an allowable radius of curvature to which the films can be subjected by measuring their mechanical properties (i.e., strain-to-failure) and linking the two.

The effort to identify an SNL-provided PVOH film with superior mechanical performance has been a consequence of a 2-year (FYs 2004 and 2005) effort. The room temperature mechanical properties of a large suite of PVOH films were first determined in FY 2004. The better performing films from that matrix then were further mechanically evaluated in FY 2005 to explore the effects of temperature on them, and that has been the focus this year.

Results

Three films were evaluated, and the following designations were used:

1. **58042**: 30 wt % Vectomer, 5 wt % 58042, and 40 wt % total solids, 225°C anneal
2. **No rubberizer**: 30 wt % Vectomer and 40 wt % total solids, 225°C anneal
3. **Brady:** 30 wt % 4010 Vectomer and 33 wt % total solids, annealed at 163°C

Film strips were cut from SNL-supplied disks or rolls into 12.7-mm widths and then tensile tested in displacement control using the test setup shown in Figure 1. Tensile load and elongation were continuously monitored.

Tensile testing was performed between room temperature (25°C) and 140°C. At least ten specimens were tested at 25°C (77°F), 60°C (140°F), and 105°C (221°F) in an attempt to generate improved statistics. Specimens were also tested at other temperatures in an attempt to identify the transition temperature between where the films failed in a brittle or ductile fashion.

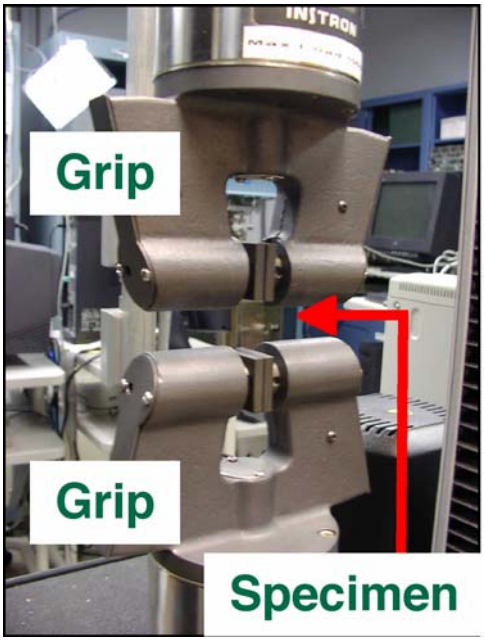

Figure 1. Tensile test setup.

Removal of the PVOH film from the Mylar carrier embrittled the film (see Figure 2), so an alternative approach was pursued to avoid embrittlement. Because the PVOH film was thin compared with the Mylar carrier, had a very weak bond with it, and had a lower strain to failure, testing commenced by testing both films in tension without removing the PVOH from the carrier. A typical measured response for this bilaminate testing is shown in Figure 3 with a characteristic load drop that is associated with the fracture of the PVOH film. This effect is also shown in Figure 4. Using classical fracture mechanics, the measured response

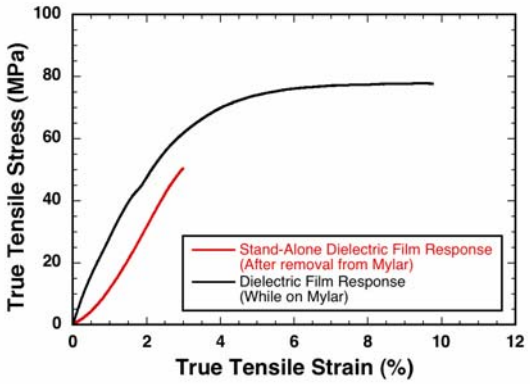

Figure 2. The act of removing the dielectric film from the Mylar carrier deleteriously affected the dielectric film, so bilaminate film testing was pursued.

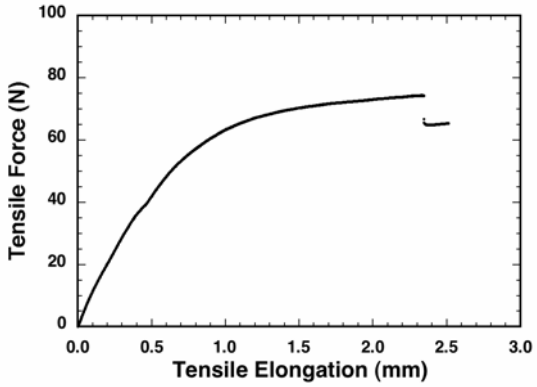

Figure 3. Example of tensile load–tensile elongation curve showing a load drop associated with the fracture of the dielectric film.

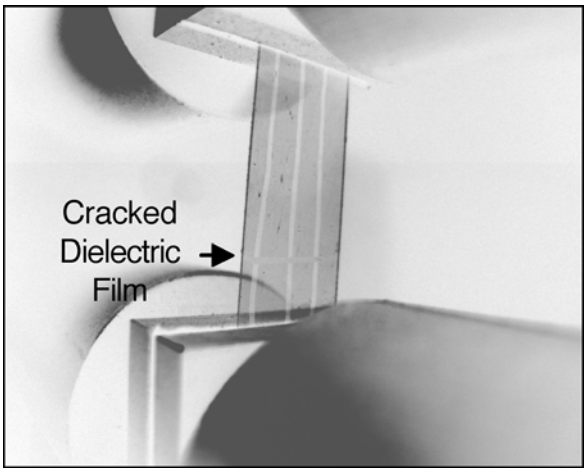

Figure 4. Fractured dielectric film shown while Mylar carrier still withstands tensile strain. The withstood load is associated with the residual load shown in Figure 3 after the load drop.

in Figure 3 can be readily deconvoluted into the Mylar and PVOH contributions that are illustrated in Figure 5, or compared as shown in Figure 6. Such an analysis was used to determine strain-to-failure as a function of temperature for the three films.

The "no-rubberizer" PVOH film composition exhibited the largest average strain-to-failure for a given temperature to 140°C, as shown in Figure 7. The bars shown in Figure 7 are standard deviations, but their presence also qualitatively indicates (brittle) fracture. For example, the no-rubberizer PVOH film fractured when tested to ~ 90°C, whereas it continued to elongate and elongate when tested above that temperature (tests were terminated if ~15% strain was accumulated without fracture). That ~90°C temperature is near the brittle-to-ductile

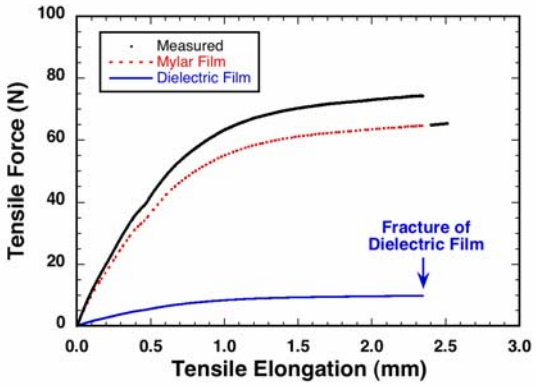

Figure 5. Deconvolution of tensile load and elongation for the dielectric and Mylar films.

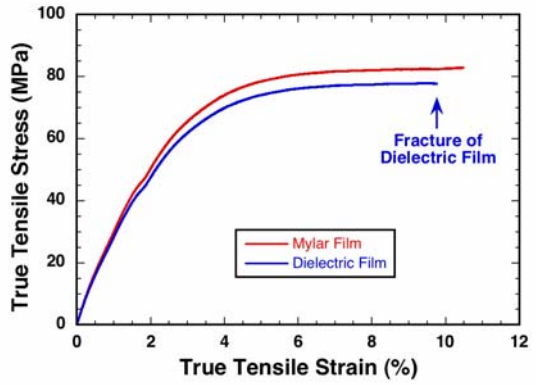

Figure 6. Stress–strain comparison of dielectric film and Mylar carrier during a test.

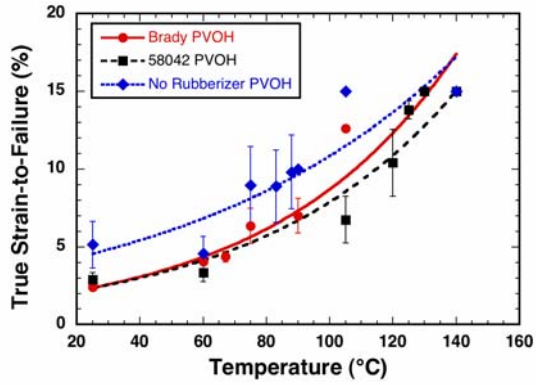

Figure 7. Tensile strain-to-failure as a function of temperature. The "no-rubberizer" composition was able to withstand larger strain-to-failure than the other two films for a given temperature up to 140°C.

transition for the no-rubberizer composition. The Brady PVOH film had a similar transition temperature, but the 58042 PVOH transition temperature neared 130°C.

The larger strain-to-failure exhibited by the no-rubberizer PVOH film means that it can be subjected to a smaller radius of curvature (R) during capacitor manufacture (see Figure 8) or service than the Brady or 58042 PVOH films when they are all subjected to the same temperature or

$$R = \frac{t}{2\varepsilon_{tens}}$$

where t is the film thickness and ε_{tens} is strain-to-failure.

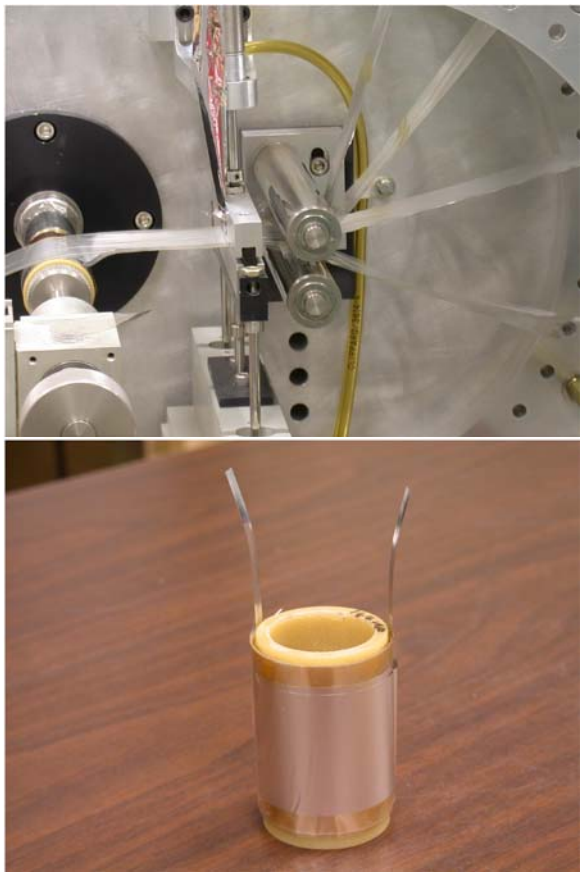

Figure 8. Dielectric films are subjected to curvature during capacitor manufacture, so it is desirable for them to be able to withstand a maximum strain-to-failure to enable more confident manufacture and smaller cylindrical capacitor diameters.

Conclusions

The PVOH film containing 30 wt % Vectomer and 40 wt % total solids, annealed at 225°C, and designated as no-rubberizer was able to withstand larger strains without failure than the 58042 and Brady PVOH dielectric films. That allows it to be successfully used in cylindrical capacitors with smaller diameters.

3. CIDI ENGINES

A. Round Pleated Ceramic Fiber Diesel Particulate Filter Cartridge Durability Improvement

Richard Nixdorf
Industrial Ceramic Solutions, LLC
1010 Commerce Park Drive, Suite I
Oak Ridge, TN 37830
(865) 482-7552; fax: (865) 482-7505; e-mail: nixdorfr@indceramicsolns.com

DOE Materials Technologies Team Leader: Rogelio Sullivan
(202) 586-8042; fax: (202) 586-1600; e-mail: rogelio.sullivan@ee.doe.gov
ORNL Technical Advisor: David Stinton
(865) 574-4556; fax: (865) 241-0411; e-mail: stintondp@ornl.gov

---

Contractor: Industrial Ceramic Solutions, Oak Ridge, Tennessee
Prime Contract No.: 4000000723
Subcontractors: Springboard Technology, Pittsfield, MA

Objectives

- Design a round pleated ceramic fiber diesel particulate filter (DPF) cartridge suitable for a heavy-duty pickup truck, using a 7.3-L Ford F250 truck as a model.
- Develop a ceramic fiber filter medium with improved strength and soot-holding capacity.
- Conduct road testing on the 7.3-L Ford truck to verify the durability and soot-loading capacity of the improved filter medium and cartridge.

Approach

- Investigate the effect on strength and soot-holding capacity of using various species of ceramic fibers and binders in the filter medium.
- Manufacture and road-test the improved cartridge system on a 7.3-L diesel vehicle to verify durability.

Accomplishments

- Improved ceramic fiber filter media burst strength from 6 to 15 psi and improved soot-loading capacity from 0.86 to 1.67 grams /ft^2.
- As a result of filter improvements, entered into a joint development program with a major diesel locomotive company to develop a commercial DPF system for locomotive engines.
- Entered into a joint development program with a worldwide Tier 1 automotive supplier to develop a commercial DPF system for the automotive market.

Future Direction

- Install a pilot production line to supply the developed DPF filter cartridges to automotive original equipment manufacturers for testing.
- Market DPF improvements worldwide to provide second-generation DPF systems to the auto industry.
- Enter a joint development agreement with a progressive exhaust system supplier to implement a more efficient DPF control system.
- Conduct high-mileage durability testing (> 100,000 miles) on the improved Industrial Ceramic Solutions (ICS) DPF cartridge.

Introduction

Diesel emissions regulations in the United States, Europe and Japan have now become a reality for all diesel engine manufacturers. Every diesel engine and vehicle supplier in the world has selected a particulate control device to comply with the 2007/2008 regulations. These wall-flow, catalyst-regenerated systems, which require high exhaust temperatures, seem to be working reasonably well in all of the application testing. The principal remaining problem is that the soot-loading capacity of the devices must be limited to avoid destruction of the filter cartridge during low-exhaust-flow regeneration. Smaller vehicles with low exhaust temperatures—such as medium-duty trucks, buses, delivery vans, pickup trucks, passenger cars, future diesel SUVs, and off-road vehicles—are also an issue. Emission control engineers are trying to avoid the need for an auxiliary-heated particulate filter that might be required to enable regeneration under all engine conditions.

Most of the problems associated with currently available extruded wall-flow ceramic filters are due to their high thermal mass and inability to conduct regeneration heat. These problems open a market opportunity for the ICS pleated ceramic fiber DPF cartridge in small diesels, 90% of the diesel engine market. Its open structure for regeneration heat release and its reduced thermal mass provide significant advantages in low-temperature exhaust systems. A number of actively heated DPFs are under development, but none have a proven record of performance, maintenance history, and desirable price for commercial diesel vehicles. ICS's completion of the FY 2005 DOE Propulsion Materials Program vehicle road test will place the ICS round pleated ceramic fiber filter cartridge high on the list of potential active and passive heated DPF systems for the next generation of products.

During FY 2004, ICS developed a round pleated DPF cartridge to control diesel particulates across all market applications. The design produced a thermal mass that is 30% that of the preferred silicon carbide wall-flow extruded ceramic filter. Experiments conducted by ICS in FY 2004 demonstrated reduced exhaust backpressure on the diesel engine from the pleated ceramic fiber DPF. This will improve engine performance and reduce the fuel penalty imposed by the particulate matter control device. The pleated ceramic fiber DPF, weighing significantly less than the extruded wall-flow filter, has a lower thermal mass to achieve lower-energy soot combustion and adds less weight to the vehicle. The open structure prevents cartridge destruction by temperature excursions when the filter is overloaded with soot. The ICS pleated ceramic fiber filter cartridge will be able to handle approximately two times the soot loading of an equivalent extruded wall-flow filter.

Approach

In FY 2005, ICS developed a round pleated ceramic fiber filter cartridge. Many experiments were conducted to determine the optimum geometry of the filter and the best means to fabricate this geometry in the laboratory. A pleating process, using a ceramic binder, was optimized. Several designs of the round pleated fiber cartridge were investigated. These prototypes are shown in Figure 1. During FY 2005, ICS developed a round pleated filter cartridge based on diesel engine testing data from our rectangular pleated filter cartridge. Extensive road testing on the Ford F250 diesel truck showed that the 7 ft^2 of media in the rectangular pleated filters is approximately 30% less than that required for optimum filter operation. ICS selected a round pleated filter approximately 6 in. in diameter and 12 in. long. This design will yield 10 ft^2 of effective filter media surface area to accommodate a

Figure 1. Round pleated filter prototypes.

full spectrum of diesel exhaust flow rates on the truck. The filter length can be reduced to 6 in. by employing the design shown in Figure 2. This design will continue to provide the 10 ft^2 of filter media required for the 7.3-L diesel engine.

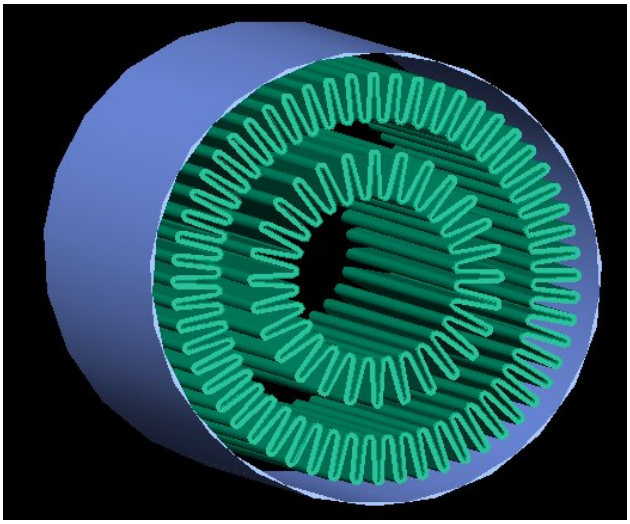

Figure 2. Round pleated filter commercial design concept,

The durability improvements achieved with FY 2005 funding were a result of investigating the ceramic binder and the ceramic fiber mix of the filter medium. Experiments were conducted in the ICS laboratory with a number of commercial binders and commercially available ceramic fibers. The binder and fiber mix was optimized in the laboratory. These improvements were transferred to commercial papermaking equipment to produce continuous rolls of filter media to be pleated and converted to pleated filter cartridges for testing. These cartridges were then road-tested on the 7.3-L Ford truck under routine driving conditions (Figure 3).

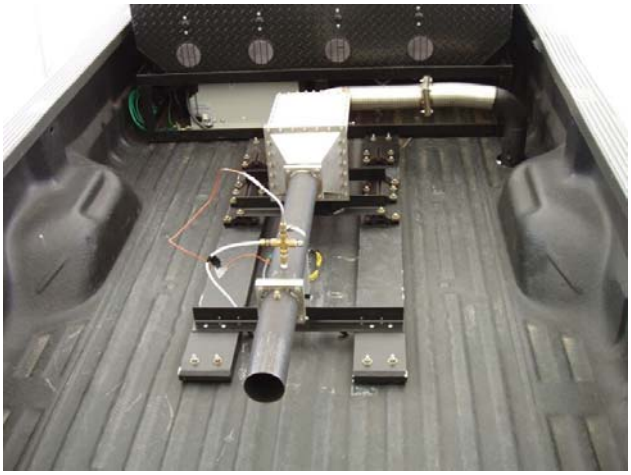

Figure 3. Road test apparatus for pleated filters,

Results

ICS was convinced that surface chemistry adjustment would improve binder adhesion to the ceramic fibers in our filter media. Beth Armstrong and Glen Kirby of Oak Ridge National Laboratory (ORNL) conducted experiments and materials analysis on the components of the ICS filter media to improve binder adhesion. The results showed ICS that surface chemistry adjustment was inadequate to achieve the 3× improvement in filter media strength that is required. This work by ORNL directed ICS to investigate other areas such as media fiber component alternatives and new papermaking techniques to obtain the needed 3× strength improvement, which eventually led to the desired results. The filter media burst strength was improved from 233 in. of water in 2004 to 415 inches of water in 2005. The burst strength improvement over the life of this program is shown in Figure 4. The soot-

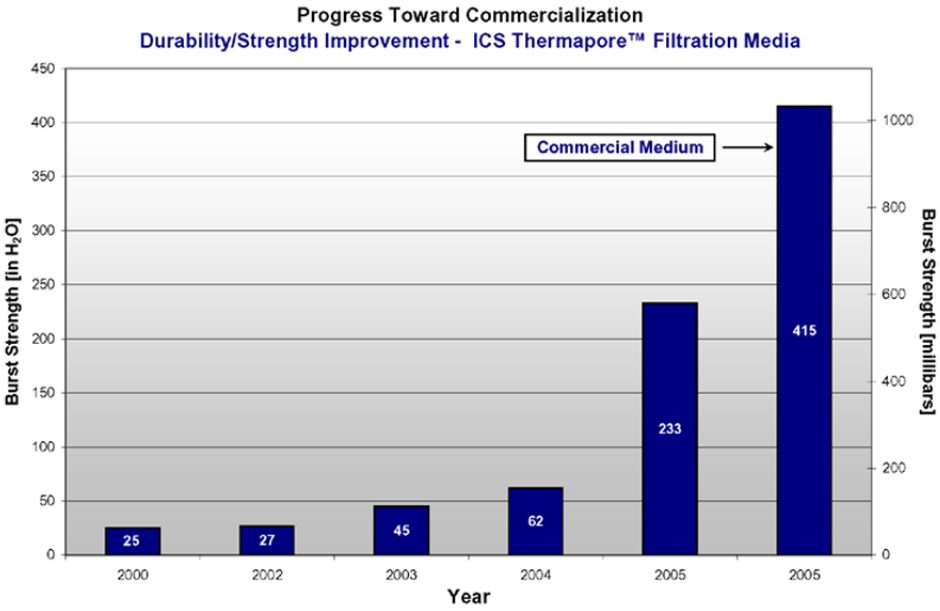

Figure 4. Filter media strength improvement.

loading capacity was increased from 0.86 g/ft^2 in 2004 to 1.86 g/ft^2 in 2005.

The improved filter media, converted to continuous paper and filter cartridges, was road-tested on the Ford 7.3-L truck. Twenty road tests were completed to load the filter to over 80 in. of water backpressure during each test. The filter was regenerated at 700°C after each road test. There was no damage to the filter cartridge during the road testing or regeneration. Figure 5 shows the clean entry and dirty exit sides of the filter prior to regeneration after the twentieth cycle.

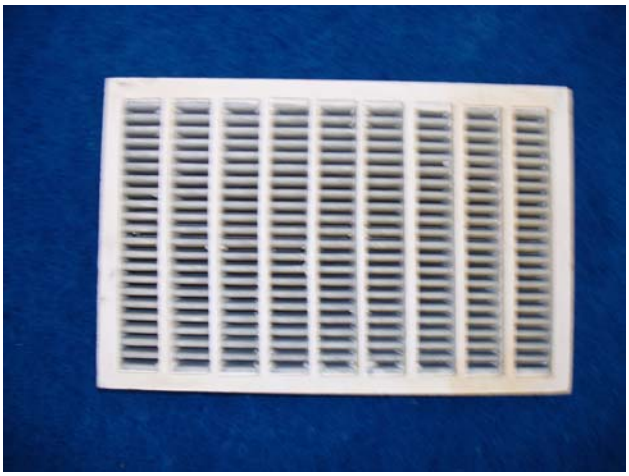

Figure 5. Twenty-cycle truck test filters.

Conclusions

The pleated ceramic fiber filter cartridge has demonstrated lower backpressure and thermal mass than conventional wall-flow DPFs. These two advantages make it a valuable addition to all types of diesel particulate matter control systems. ICS is working with a major international filter manufacturer to license the use of the technology to supply the large volume of filter cartridges necessary to supply the worldwide diesel industry. It is also working with several vehicle manufacturers to develop improved commercial exhaust control systems. The gasoline engine catalytic converter was introduced in 1975; in 2005, it is just reaching a stage of optimum efficiency. The selected diesel engine DPF control systems will be installed on diesel vehicles in 2006. These systems have an unproven operating record in volume use. There is significant opportunity for improved technologies to enter the commercial marketplace. The advantages offered by the ICS DPF technology will be a contributor to optimization of the diesel emission control systems.

Publications/Presentations

"Round Pleated Ceramic Fiber Filter," presented at the DEER Conference, Chicago, August 2005.

"Advances in Filter Media Development for Diesel Exhaust Systems, Ceramic Bonded Ceramic

Fiber Pleated DPF Cartridge" presented at the American Filtration and Separation Society Diesel and Gas Engine Emissions Solutions Conference, Ann Arbor, MI, September 2005.

Awards/Patents Issued

"Ceramic and Fiber-Based Filter Web and Method," U.S. Patent 6,913,059 B2, July 2005.

B. Fabrication of Small Fuel Injector Orifices

John B. Woodford, George R. Fenske
Argonne National Laboratory
9700 South Cass Avenue
Argonne, IL 60439
(630)252-0910; fax (630)252-4798; e-mail gfenske@anl.gov

DOE Technology Development Manager: Rogelio Sullivan
(202) 586-4082; fax: (202) 586-1600; e-mail: rogelio.sullivan@ee.doe.gov

Contractor: Argonne National Laboratory, Argonne, Illinois
Prime Contract No.: W-31-109-Eng-38

Objectives

- Develop a methodology for reducing the diameter of fuel injector orifices to 50 μm by applying material to the internal diameter (ID) of the orifice. Smaller orifices should improve fuel distribution, improve efficiency, and reduce emissions.
- Characterize the spray and combustion properties of the fuel injector system coated with electroless nickel (EN).
- Transfer the developed technology to DOE industrial partners.

Approach

- Transfer EN plating deposition technology for reducing the orifice diameter to a commercial plating company.
- Evaluate the potential of EN plating for improving surface finish and reducing deposit formation on injector nozzles.

Accomplishments

- Devised a new approach for preparing test nozzles in concert with the U.S. Environmental Protection Agency–National Vehicle and Fuel Emissions Laboratory (EPA-NVFEL). Also initiated collaboration with a major fuel injector manufacturer for further engine testing of plated nozzles for deposit mitigation.
- In concert with Imagineering, Inc., a commercial plating company, developed a method for improving the surface finish of commercial-scale-plated nozzles.
- In the area of deposit formation testing, refined the test method to include examination of oxidative volatiles and characterized the effect of phosphorus levels in the EN plating on deposit formation. Provided alloy samples for testing to Pennsylvania State University and began to work with Northern Illinois University (NIU) on studying this issue.

Future Direction

- Characterize spray characteristics of coated injectors in collaboration with Argonne National Laboratory–Energy Systems (ANL–ES) and ANL–Advanced Photon Source (ANL–APS).
- Provide coated injector tips to EPA-NVFEL personnel for spray characterization and combustion tests.
- Apply advanced characterization methods for detailed examination of surface chemistry during deposit formation, particularly extended X-ray absorption fine structure (EXAFS).

Introduction

In 2007, EPA regulations mandate diesel engine emission reductions to 0.01 grams of particulate matter (PM) per engine horsepower per hour and 0.2 grams of nitrogen oxides (NO_x) per engine horsepower per hour. Further reductions are expected for 2010. In order to achieve these levels, engines are being redesigned to reduce in-cylinder soot production. One design change under consideration is the reduction of the fuel injector orifice diameter.

Pickett and coworkers[1,2] have shown elimination of soot in a test cylinder by reducing the injector orifice diameter to 50 μm, even with high levels of exhaust gas recirculation, and concomitant reduction in NO_x emissions. NVFEL researchers have observed reduced PM emissions from a light-duty diesel engine equipped with 75-μm-diameter injector orifices. These reductions arise from increases in fuel atomization efficiency, leading to more complete combustion.[3] Although it is currently possible to economically mass-produce injectors with 100-μm diameter-orifices using electrodischarge machining, further reductions in hole size are accompanied by unacceptable fabrication error rates at this point.

Reducing orifice diameter carries with it a number of penalties, however. It is inevitable that a marked reduction in orifice area (e.g., from 150 to 50 μm) will lead to a reduction in the amount of fuel that can be delivered to the combustion chamber without increasing the number of spray holes, the injection pressure, and/or the discharge coefficient. The potential impact of coking on smaller orifices is also much greater, as smaller holes will be more readily blocked by coking deposits on the injector tip and in the spray holes themselves. Coking deposits are a particular problem with tapered-orifice nozzles, another technique for increasing fuel atomization and thus reducing PM emissions.

Another issue is alternative fuels. One method to minimize dependence on foreign oil is the increased use of bioderived fuels such as vegetable oil esters. Because of the presence of carbon-carbon double bonds in the carboxylic acid chain precursors, these fuels readily form coking deposits in the combustion chamber—a major problem in concert with smaller spray holes. Other alternative fuels include alcohols such as methanol or ethanol. These are not typically used neat but are blended with conventional diesel fuel. One emissions reduction strategy is to inject an ethanol/water mixture along with conventional fuel, reducing combustion temperature and NO_x emissions. However, alcohol partial oxidation products can include corrosive carboxylic acids, which will damage the steel nozzles over time.

In concert with more commonly-used fabrication techniques, EN plating has been used to prepare fuel injector nozzles with orifice diameters as small as 50 μm. EN plating also promises to mitigate or solve all of the difficulties described above: It is corrosion-resistant; plated surfaces are smoother than unplated surfaces; it increases the discharge coefficient of the plated orifices; and it can be used to deposit a wide variety of alloys, offering the possibility of tailoring surface chemistry to reduce or eliminate deposit formation.

Approach

As described in previous reports, the reduction of orifice diameter is accomplished by coating the orifice interior with EN plating. EN plating is a method of depositing nickel/phosphorus or nickel/boron alloys onto metallic surfaces from aqueous solution. This approach has been successfully used in previous years to reduce orifice diameter from 200 to 50 μm on a bench scale, and from 180 to 75–80 μm on a commercial scale. Other metal alloys have been deposited using the same principle.

Having demonstrated that it is possible to use EN plating to reduce orifice diameter to the desired size, the next goal is to demonstrate the usefulness of EN-plated nozzles for solving the problems described in the Introduction: improving spray properties and discharge coefficient, reducing deposit formation, and resisting corrosion.

Results

The critical milestone for this project has been to characterize the spray properties and engine performance of plated nozzles. Efforts to that end are progressing. These include collegial agreements with EP-NVFEL to evaluate plated nozzles in a 4-cylinder light-duty engine, as well as with a major light-duty injector manufacturer to evaluate deposit formation properties of EN-plated nozzles. Internal R&D funds have also been solicited to perform optical and X-ray imaging studies of plated nozzle fuel sprays. The latter studies will cover a range of

orifice diameters and fuel types, including conventional diesel, bioderived diesel, and ethanol blends.

One of the issues raised in the FY 2004 report was the finish on surfaces plated by Imagineering (Figure 1a). That issue has been resolved (Figure 1b). The company's method of removing EN from a plated surface without damaging the substrate did not work for keeping the needle guide free of plating, however (cf. Figure 2), and its use of conventional maskants on the guide area did not allow sufficient plating bath flow to coat the orifices uniformly. Imagineering suggested that the plating be removed mechanically, as EN plating can be ground off. This proved to be feasible. The same approach can be used to remove overcoating from the needle seat area (cf. Figure 3), which might otherwise adversely impact needle sealing.

These issues all arise from the use of existing nozzles with matching needles. In production, it is anticipated that needles and nozzles will be ground and lapped after plating. Thus no net cost or increase in time will accrue from the machining, and the only increases in cost will be from the plating process itself.

Deposit formation tests using the test method developed two years ago, dropping diesel fuel onto heated plated and unplated surfaces, are continuing. The test protocol has been expanded to include different materials, EN compositions, and temperatures of 200, 250, and 300°C. The test method has also been refined for use with less-volatile fluids, in this case a high-oleic-content sunflower oil lubricant. This has been done as a worst case for deposit formation, in that the oil has a large number of carbon-carbon double bonds and contains no antideposit additives. By weighing the samples before and after heating, and again following rinsing with hexane, the mass loss due to the formation of volatiles by oxidative cleavage can be decoupled from the mass gain due to deposit formation.

Figures 4 and 5 are plots of deposit mass gain and volatiles mass loss from tests of nickel and EN plating with three different phosphorus concentrations at 250°C. The mid-phosphorus plating is similar to the commercial plating bath that was used for previous tests. Although there is considerable scatter in the data, it is clear that all of these are superior to unplated steel, and that the mid-phosphorus coating is actually inferior in deposit resistance to the low- and high-phosphorus coatings. Figure 6 is a plot of deposit mass for diesel tests with the different EN plating compositions at different temperatures. At lower temperatures, all of the plating compositions are superior to unplated steel, but at 300°C only low-phosphorus EN is still

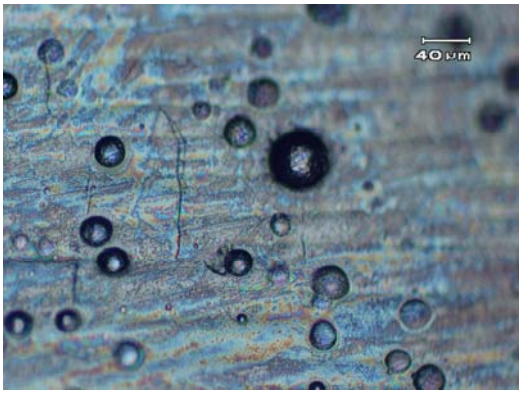

(a)

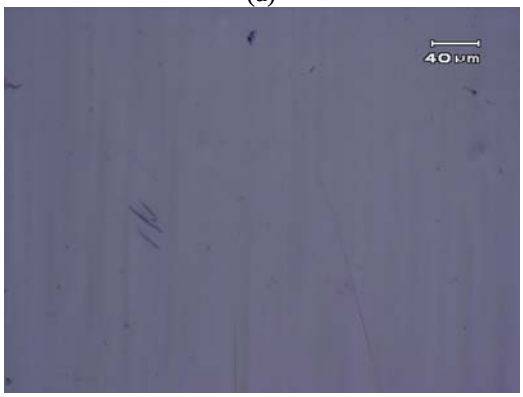

(b)

Figure 1. Optical micrographs of injectors plated at Imagineering early last year (a) and late last year (b), showing differences in surface finish.

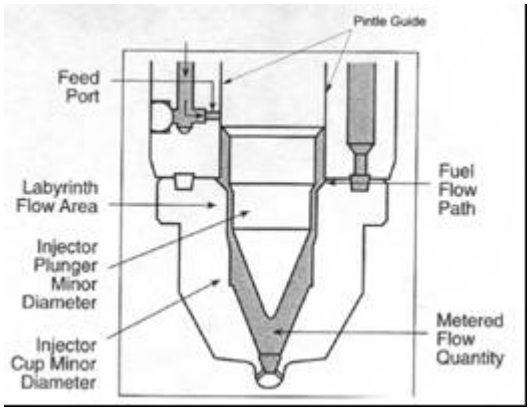

Figure 2. Plan sketch of nozzle, indicating the pintle guide area.

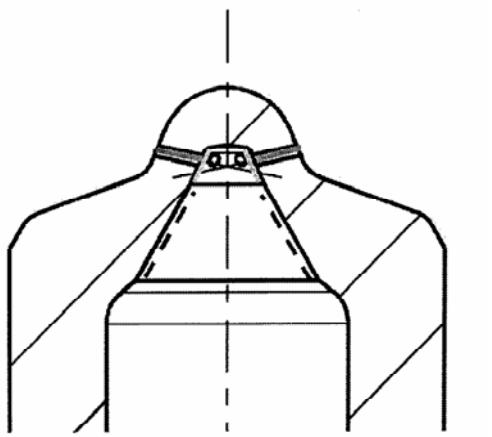

Figure 3. Plan sketch of nozzle tip region, indicating the needle seat area.

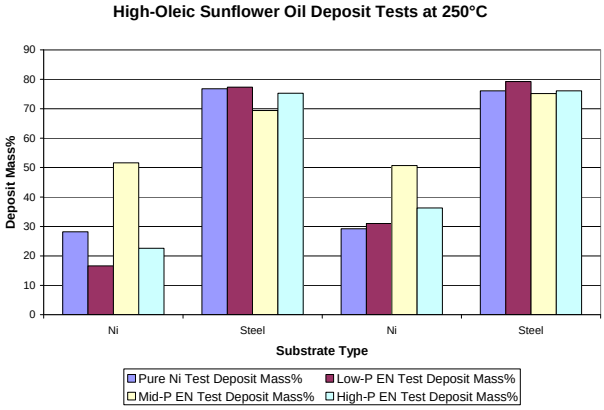

Figure 4. Deposit mass % on nickel, EN plating with different levels of phosphorus, and unplated steel following deposit tests with sunflower oil at 250°C.

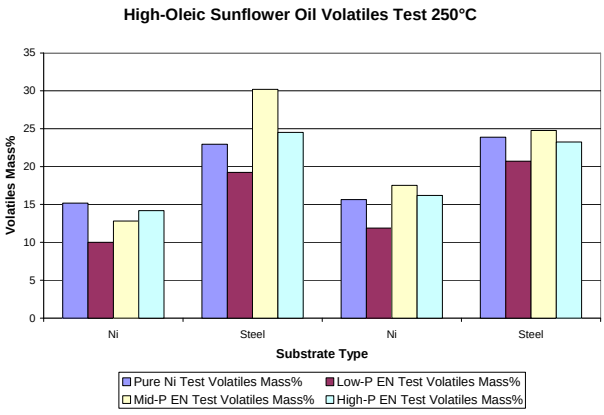

Figure 5. Volatiles mass % on nickel, EN plating with different levels of phosphorus, and unplated steel following deposit tests with sunflower oil at 250°C.

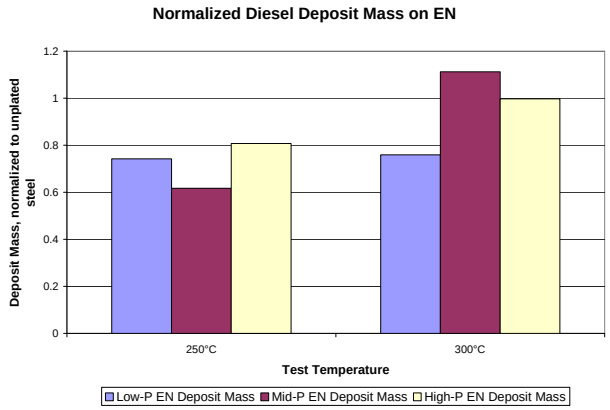

Figure 6. Diesel deposit mass on the different EN compositions at different temperatures, normalized to deposit mass on unplated steel in the same tests.

better than steel. Considering the scatter in the data, the other two compositions are no worse than steel, though. This contrasts sharply with another corrosion-resistant alloy, 304 stainless steel (Figure 7). Although stainless steel is superior to mild steel at 200°C, at higher temperatures it is markedly inferior to mild steel. The reason for this is not fully understood, but it may relate to the catalytic activity of chromium ions in fuel oxidation. Further investigation was undertaken, as will now be detailed.

According to Cochrac and Rizvi,[4] partial oxidation is catalyzed by the presence of metal carboxylates, and they gave an example of the catalytic activity of iron octanoate. In the past year, deposit test sample dishes made from mild steel and stainless steel have been sent to Professor Charles Johnson of NIU and APS, for Mößbauer

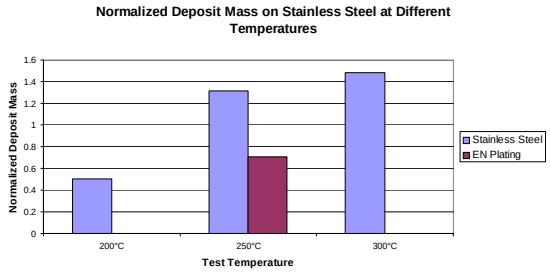

Figure 7. Diesel deposit mass on stainless steel at different temperatures, normalized to deposit mass on mild steel in the same tests. Normalized deposit mass for commercial mid-phosphorus EN at 250°C is shown for comparison

spectroscopy. This technique is used to measure the oxidation state of iron in the near-surface region of the sample. Comparing mild steel and stainless steel will determine if any iron ions are present in the stainless steel deposit.

In other tests, the effect of surface finish on deposit formation has been examined (Figure 8). No consistent influence was seen in the initial tests, but they will be repeated in more detail in the next year. A test has been performed using Fischer-Tropsch synthetic diesel fuel (Figure 9), which is free of detergent additives, sulfur, and aromatic compounds. As expected, total deposit mass is lower, but the superiority of EN plating over steel is also more pronounced.

The data from Professor Joseph Perez's prior tests have been revisited and analyzed in greater detail, particularly the gel permeation chromatography results (Figure 10). These show the distribution of molecular weights in the apparently-unreacted oil following the PSMO tests.

Little change in average molecular weight of the oil over the course of the test indicates that little partial oxidation has taken place. High-molecular-weight species are deposit precursors created by incomplete oxidation of the test fluid. Apparently, although a substantial amount of deposit precursors builds up in the oil over the EN-plated surfaces, it does not condense into insoluble deposits very readily. The reason for this is unclear. As a result of PSMO tests on other coating materials, NiMo, NiCu, and NiMoCu coatings have been produced and provided to Professor Perez. The results are forthcoming.

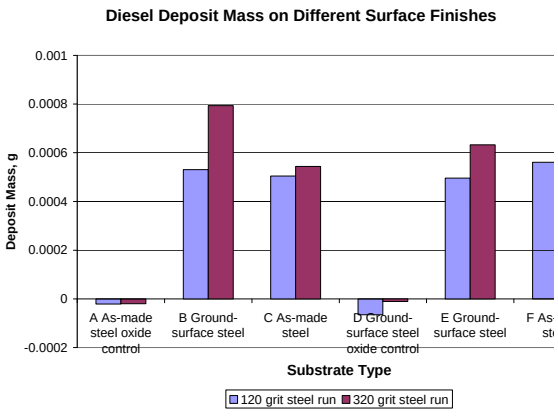

Figure 8. Diesel deposit mass on mild steel at 250°C after roughening with different grades of silicon carbide abrasive paper.

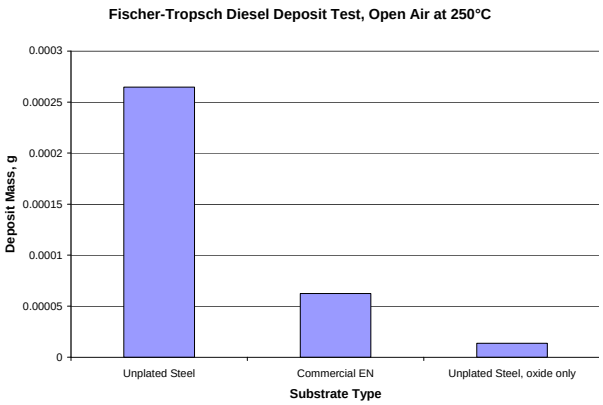

Figure 9. Fischer-Tropsch synthetic diesel deposit mass on EN plating and steel at 250°C.

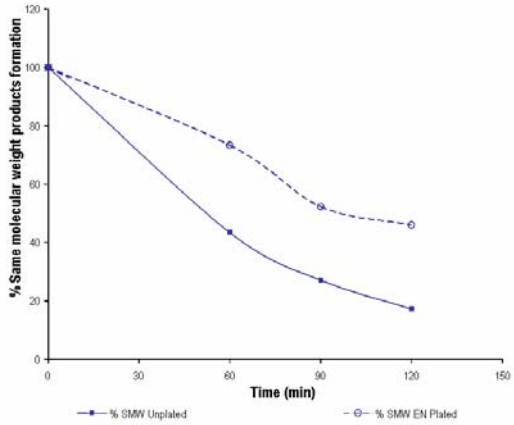

(a)

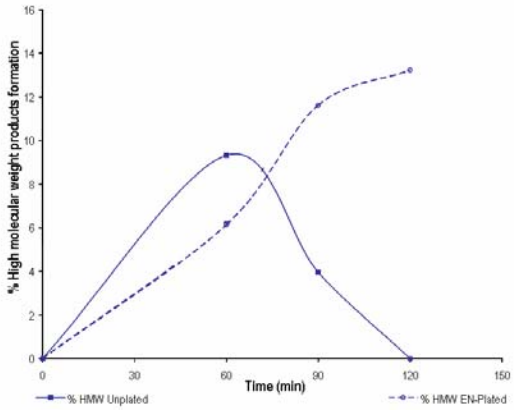

(b)

Figure 10. Plots of same-molecular-weight fraction (a) and high-molecular-weight fraction (b) as a function of time on unplated and EN-plated steel surfaces.

Conclusions

A candidate method has been developed for fabricating nozzles for spray testing, and arrangements have been made with EPA-NVFEL and a major fuel injector manufacturer to perform engine tests in the next year. Imagineering has been able to provide plated nozzles with satisfactory surface finishes as well. In the area of deposit analysis, the Mößbauer spectroscopy work performed in concert with Northern Illinois University will provide baseline data to apply to a more detailed surface analysis of deposits using EXAFS to determine oxidation state and local bonding structure around different elements in the coatings. In-house deposit tests have begun to elucidate the relationship between phosphorus level in the plating and deposit formation propensity.

References

1. Lyle M. Pickett and Dennis L. Siebers, Paper No. 2001-ICE-399, ICE Vol. 37-1, 2001 Fall Technical Conference, American Society of Mechanical Engineers 2001, ed. V.W. Wong.
2. L.M. Pickett, D.L. Siebers, A.F. Morales, J. Hachman, and A.K. Sinensky, "An Investigation of Diesel Soot Formation Processes Using High Aspect Ratio Micro-Orifices," presented at HARMST 2003 High-Aspect Ratio Micro-Structure Technology Workshop, Monterey CA, 2003.
3. John B. Heywood, *Internal Combustion Engine Fundamentals*, McGraw-Hill, 1988.
4. G. Cochrac and S.Q.A. Rizvi, "Oxidation of Lubricants and Fuels", Chapter 30 in *Fuels and Lubricants Handbook*, ed. G.E. Totten, American Society for Testing and Materials, 2003.

Publications and Presentations

J. Woodford, J.M. Perez, and G. Fenske, *Deposit Formation on Electroless Nickel*, in press

Poster, DOE Advanced Combustion Engine R&D Merit Review, April 19–21, 2005, Argonne National Laboratory

C. Electrochemical NO_x Sensor for Monitoring Diesel Emissions

L. Peter Martin, Seung Wan Song, and Robert S. Glass
Lawrence Livermore National Laboratory
P.O. Box 808, MS L-353
Livermore, CA 94551-0808
(925) 423-7140; fax: (925) 423-7914; e-mail: glass3@llnl.gov

DOE Materials Technologies Team Leader: Rogelio Sullivan
(202) 586-8042; fax: (202) 586-1600; e-mail: rogelio.sullivan@ee.doe.gov

Contractor: Lawrence Livermore National Laboratory, Livermore, California
Prime Contract No.: W-7405-Eng-48

Objectives

- Develop a compact, rapid-response electrochemical nitrogen oxide (NO) or total nitrogen oxides (NO_x) sensor for compression-ignition, direct-injection (CIDI) exhaust gas monitoring.
- Collaborate with the Ford Research Center and Oak Ridge National Laboratory to optimize sensor materials, operating parameters, and performance.
- Identify materials issues pertaining to aging and performance for candidate sensor materials.

Approach

- Use an ionic (O^{2-}) conducting ceramic as a solid electrolyte and a catalytic metal oxide as a working electrode.
- Apply a constant voltage- or current-bias (through the electrolyte) between a working and counter electrode.
- Correlate the NO_x concentration with the current-voltage behavior of the sensor.
- Evaluate sensing mechanism and aging during operation using electrochemical and analytical techniques.

Accomplishments

- Identified aging processes in strontium (Sr) -doped $LaCrO_{3-\delta}$ (LSC) perovskite electrodes.
- Gave an invited presentation at the 207th meeting of the Electrochemical Society, Quebec, May 2005.

Future Direction

- Continue to explore materials issues related to sensitivity and stability by investigating sensing mechanisms using electrochemical and analytical techniques and by evaluating microstructural evolution during sensor aging.
- Evaluate cross-sensitivity to important redox gases and perform dynomometer testing.
- Demonstrate the commercialization potential of the current-biased sensor technique.
- Transfer the technology to a commercial entity.

Introduction

Increasingly stringent emissions regulations will require the development of comprehensive on-board diagnostic systems for exhaust-gas monitoring and feedback control of regulated pollutants, including hydrocarbons, carbon monoxide, and NO_x. For example, an on-board NO_x sensor will be needed to monitor the regeneration of the NO_x reduction catalyst in the next generation of CIDI engines. To that end, NO_x sensors based on ionically-conducting, solid-state electrochemical devices have been proposed.[1,2] Typical operating conditions for these sensors can include elevated O_2 concentrations of 5–15%, temperatures in the range of 600–700°C, and NO_x concentrations in the range of 10–1000 ppm.[3–5] Strontium-doped $LaCrO_{3-\delta}$ (LSC) perovskite has been identified as a potential NO_x sensor electrode when coupled with a yttria-stabilized zirconia (YSZ) electrolyte.[6,7] Other perovskite-type metal oxides such as $LaFeO_3$ and Sr-doped $LaCoO_3$ have also been investigated as NO_x sensor electrodes.[8]

The NO_x sensing performance of these electrode materials is strongly dependent on microstructure; however, quantifying this dependence is not straightforward. In addition, electrode performance often changes significantly with extended operation (aging). Aging can affect the particle morphology, stoichiometry, and electrode-electrolyte interface structure. A better understanding of these effects is required for optimization of sensor performance and long-term reliability. While there have been few, if any, reported investigations of the aging behavior of these materials as sensor electrodes, there is a substantial body of literature describing aging effects in related solid oxide fuel cell cathode materials.[9,10] Those reports describe significant cathodic polarization and aging effects and suggest a strong need for systematic analyses of the aging processes in perovskite materials used as sensor electrodes.

In this work, LSC/YSZ/platinum (Pt) electrochemical cells were prepared in a three-electrode configuration by depositing LSC working electrodes (WE) and Pt counter (CE) and reference (RE) electrodes on sintered YSZ electrolyte substrates. LSC electrodes were prepared from $La_{0.85}Sr_{0.15}Cr_{1.01}O_3$ powder sintered at 1200°C, while Pt electrodes were prepared from a commercial Pt ink sintered at 1000°C. Selected cells were electrochemically aged at 600–700°C in 10% O_2 and 0–500 ppm NO_x by applying a positive bias of 250 mV to the LSC WE (relative to the Pt reference electrode). Detailed characterization of the electrodes—using scanning electron microscopy (SEM), X-ray photoelectron spectroscopy (XPS), and X-ray diffraction (XRD)—was used to elucidate the effects of aging. The effects of the observed aging processes were evaluated with respect to the electrochemical performance and NO_x sensing characteristics of the cell. Before proceeding further with the development of prototypes for more advanced testing, it is necessary to develop a thorough understanding of materials aging and electrochemical properties for LSC and other prospective sensor materials.

Results

SEM was used to examine both the un-aged and aged electrodes to characterize the morphology and porosity and to evaluate any changes due to aging. Figure 1(a) shows the surface of a typical un-aged LSC electrode. The LSC is porous and consists of

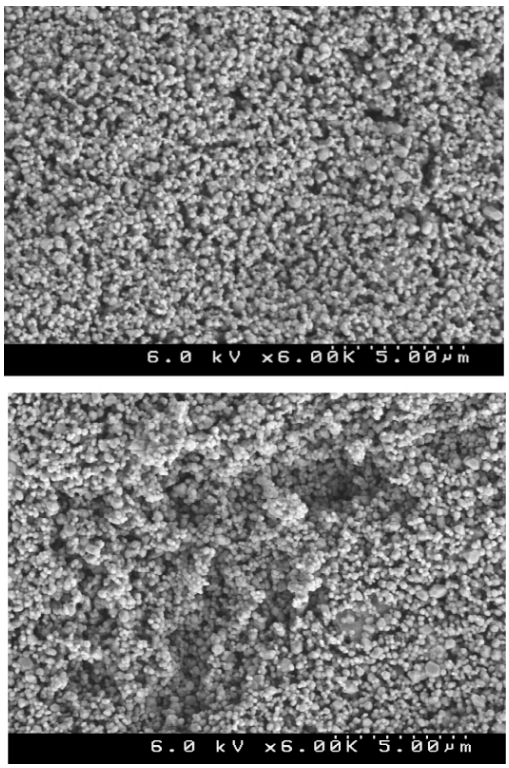

Figure 1. (a) SEM image of the surface of an un-aged LSC electrode. (b) SEM image of the surface of an LSC electrode aged for one week in 10% O_2 at 600ºC.

particles ranging from ~100–500 nm in size. After aging at 600°C, numerous cracks appear at the electrode surface (Figure 1b). Higher-magnification images show that the average particle size increases slightly. The origin of the surface cracks is not currently understood; however they do not develop in LSC electrodes aged in the absence of applied bias, suggesting that the current flow through the cell has a significant effect on their evolution.

XRD patterns for LSC electrodes sintered onto the YSZ substrate before aging show an impurity phase that is believed to be $SrCrO_4$. This is consistent with prior reports indicating that $ACrO_4$ (A=Ca, Sr) is often present in doped lanthanum chromites. After aging at 700°C, there are indications of the formation of $SrZrO_3$. It is postulated that the $SrZrO_3$ forms as a result of a reaction between $SrCrO_4$ and Zr at the YSZ-LSC interface. The formation of an $SrZrO_3$ reaction product is limited by the availability of the $SrCrO_4$ impurity at or near the interface. Also apparent in the pattern for the aged electrode is a splitting and sharpening of the peaks at high 2θ. This indicates grain coarsening consistent with the particle growth observed in the SEM images.

Detailed surface composition analyses were performed on the LSC electrodes, before and after aging at 600-700°C, using XPS. The results are shown in Table 1. These data indicate that the surface of the un-aged LSC is initially O-rich and Sr-rich. They deviate significantly from the theoretical values obtained based on the chemical formula $La_{0.85}Sr_{0.15}Cr_{1.01}O_{3-\delta}$. Table 1 also shows the surface composition after aging at 600°C under both anodic and cathodic polarization. The most notable effect is that the O-content at the surface decreases under cathodic polarization and increases under anodic polarization. In addition, there is some indication of changing La/Sr stoichiometry with the bias direction.

Ar-ion sputtering was used to remove the electrode surface, exposing the subsurface for XPS analysis. In contrast to the surface, the bulk of the LSC is relatively stoichiometric. For the un-aged LSC, the material is approximately stoichiometric at a depth of ~28 nm below the surface. After anodic aging, however, the chromium and lanthanum contents approach the theoretical values more quickly with depth, ~12–16 nm. This occurs despite the fact that the surface is still highly nonstoichiometric, as discussed earlier.

Table 1. Surface atomic ratios from the XPS for the LSC before and after aging at 600°C

		Polarization		
Ratio	**Theory**	**Un-aged**	**Anodic**	**Cathodic**
O/La	~3.5	6.8	9.7	5.0
O/Cr	~3	5.1	6.3	4.0
Cr/La	1.2	1.3	1.6	1.2
La/Sr	5.7	1.2	1.3	2.5
Cr/Sr	6.7	1.6	2.1	3.0

In an attempt to gain insight into the practical effects of long-term aging on NO_x sensing performance, an LSC/YSZ/Pt cell was evaluated for its response to varying NO_x concentrations during long-term aging in 10% O_2. Figure 2 compares the NO_x response of the cell before and after anodic polarization at 600°C for 15 days. Note that this cell was designed to allow evaluation of the electrode response for obtaining purely mechanistic information and was not configured for optimal performance as an actual sensor. Before aging (i), the baseline was unstable and the NO_x response was poor, particularly to NO. After aging (ii), the baseline stabilized, and both the NO and NO_2 response became significantly enhanced. In addition, the NO_x response time improved significantly over the duration of the experiment. These results underscore that aging of the NO_x sensing electrodes is crucial for obtaining stable and reproducible behavior. Similar remarks may also pertain to sensors for other gases, although different aging characteristics may be evident.

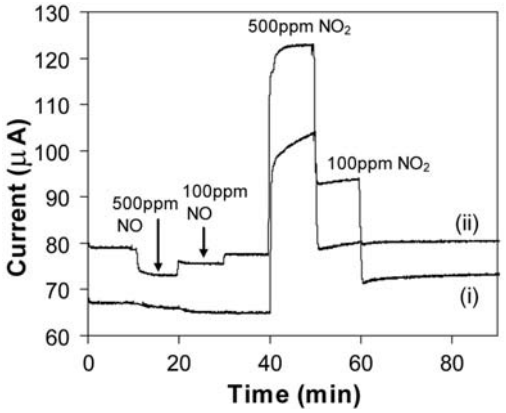

Figure 2. Cell performance before (i) and after (ii) aging for 15 days at 600°C in 10% O_2.

Conclusions

The performance of metal oxide electrodes proposed for use in electrochemical NO_x sensors is highly dependent upon microstructure and surface stoichiometry, which are influenced by aging in test gas atmospheres. This is particularly true in the case of doped perovskites, which are known to be potentially non-stoichiometric. Currently, LSC is being evaluated as a potential sensor electrode material. For this material in particular we have noted significant aging-related microstructural and chemical changes when it is tested under simulated operating conditions. This aging is not necessarily deleterious, and in fact seems to improve the NO_x sensing performance. The findings are significant, however, in that they demonstrate the need for careful pre-aging (i.e., burn-in) of the sensors before use and demonstrate that performance characteristics reported prior to aging may not be representative of real-world sensor performance.

References

1. N. Miura, G. Lu, and N. Yamazoe, *Solid State Ionics* **136**–137, 533 (2000).
2. W. Gopel, R. Gotz, and M. Rosch, *Solid State Ionics* **136**–137, 519 (2001).
3. F. Menil, V. Coillard, and C. Lucat, *Sensors and Actuators B* **67**, 1 (2000).
4. J. Kaspar, P. Fornasiero, and N. Hickey, *Catal. Today* **77**, 419 (2003).
5. M. Zheng, G.T. Reader, and J.G. Hawley, *Energy Convers. Management* **45**, 883 (2004).
6. D.L. West, F.C. Montgomery, and T.R. Armstrong, *Sensors & Actuators B* **106**, 758 (2005).
7. I.V. Bruser, U. Lawrenz, S. Jacobs, H.-H. Mobius, and U. Schonauer, S*olid State Phenomena* **39**–**40**, 269 (1994).
8. M.L. Grilli, E.D. Bartonlomeo, and E. Traversa, *J. Electrochem. Soc*. **148**, H98 (2002).
9. S.P. Jiang and J.G. Love, *Solid State Ionics* **158**, 45 (2003).
10. H.Y. Lee, W.S. Cho, S.M. Oh, H.D. Wiemhöfer, and W. Göpel, *J. Electrochem. Soc*. **142**, 2659 (1995).

Publications/Presentations

"Aging Studies of Sr-doped LaCrO3/YSZ/Pt Cell for a NO_x Sensor," presented at the 207th meeting of the Electrochemical Society, Quebec City, Canada, May 18, 2005.

"Aging Studies of Sr-doped $LaCrO_3$/YSZ/Pt Cells for an Electrochemical NO_x Sensor," in preparation, to be submitted to *The Journal of the Electrochemical Society*.

D. Hydrogen Compatibility of Materials for Automotive Applications

James Holbery, Chuck Henager, Stan Pitman, Russ Jones, and Thomas Gallant
Pacific Northwest National Laboratory
P.O. Box 999
Richland, Washington 99354
(509) 375-3686; fax: (509) 375-2379; e-mail: james.holbery@pnl.gov

Peter Blau, Laura Riester
Oak Ridge National Laboratory
Oak Ridge, TN 37831
(865) 574-5377; fax: (865) 574-6918; e-mail: blaupj@ornl.gov

DOE Materials Technologies Team Leader: Rogelio Sullivan
(202) 586-8042; fax: (202) 586-1600; e-mail: rogelio.sullivan@ee.doe.gov

Contractor: Pacific Northwest National Laboratory, Richland, Washington
Prime Contract No.: DE AC06 76RLO 1830

Objectives

- Measure the friction and wear characteristics of injector materials in hydrogen environments.
- Measure the performance of actuators and actuator materials in hydrogen environments.

Approach

- Use atomic force microscopy (AFM) and nanomechanical measuring techniques to evaluate the friction and wear characteristics of injector materials in hydrogen environments.
- Perform in situ voltage/current pulses of fuel injector actuators in high-pressure hydrogen gas simulating engine conditions.

Accomplishments

- Completed the design, construction, safety check, and full operation of a high-pressure hydrogen test apparatus for actuator and injector materials, including a complete system for in-situ monitoring of piezo materials.
- Conducted AFM and nanomechanical testing on “as-received” and hydrogen-exposed injector materials and showed that the friction coefficient increases with H_2 exposure, largely as a result of surface facet formation, and is not limited to one material system.
- Conducted multi-pass friction tests at constant load that indicate a significant increase in coefficient of friction, with indications of wear track and third-body contributions.

Future Direction

- Evaluate the durability of needle-nozzle engine materials as a result of service within a hydrogen environment, including hydrogen diffusion, barrier coatings, and material selection.
- Evaluate new coatings, alloys, and piezo barrier materials under hydrogen service environments.
- Evaluate sliding and impact wear, with special attention to surface galling, to determine needle-nozzle long-term durability.
- Develop concepts for an engineering wear simulation test in high-pressure hydrogen.

Introduction

The friction and wear characteristics of metallic materials depend largely on surface oxide films. However, a hydrogen environment is chemically reducing, so the loss of the surface oxide by wear will result in bare surface contact and an increase in friction and wear. An exploratory study was undertaken to determine the frictional behavior of metals in a hydrogen environment using in situ AFM/friction force microscopy and nanoindentation–nanoscratch measurement. Measurements were made in a hydrogen environment on metallic injector materials used by Westport Innovations, Inc. and materials analysis was conducted on the relevant material features.

Piezoelectric actuators use the piezoelectric materials PZT, which is lead and zirconium titanate embedded in epoxy or other polymer materials. Potential degradation mechanisms include changes in the capacitance[1–3] and cracking[4] of the PZT material, separation of the PZT wafers within the stack, loss of electrical contact, or degradation of the epoxy or polymer holding the PZT materials. Any of these processes will result in loss of performance. Tests were conducted on actuators and PZT material in a high-pressure hydrogen environment at up to 100°C, typical of conditions in engine applications. The actuators were monitored during in situ voltage cycling that matches the actuator conditions.

Surface Properties of Injector Materials in Hydrogen

Hydrogen internal combustion engines have four primary types of fueling systems, including carburetion, throttle body-injection, intake port fuel injection (PFI), and direct in-cylinder injection. While PFI offers very good cylinder-to-cylinder fuel distribution, minimum fuel charge in the intake manifold, and low cost, there is still much to learn pertaining to the details of using PFI equipment for direct injection in a hydrogen fuel environment.[5]

This study aims to better understand and quantify the mechanisms that determine friction coefficient and surface properties of injector needles and nozzles within a 100% hydrogen service environment by comparing hydrogen-exposed and "as-received" actuator materials. These are needle and nozzle designs; the corresponding material information is listed in Table 1 for two materials, J2 and S1.

Table 1. List of injectors and corresponding material specifics in the test matrix

Injector name	Component	Material
No. S1	Needle	Carburizing steel
No. S1	Nozzle	Carburizing steel
No. J2	Needle	AISI M2
No. J2	Nozzle	AISI H13

Using a combination of nano-mechanical measurement techniques combined with experimental analysis, we analyzed the effects of hydrogen on needle and nozzle materials with the purpose of determining sliding contact degradation and extended wear behavior.

Nanomechanics

Nanoindentation and scratch friction measurements were conducted with a conical diamond tip with a tip radius of approximately 400 nm. Working in conjunction with Peter Blau and Laura Reister of Oak Ridge National Laboratory, we used a state-of-the-art Hysitron® Nanoscratch® apparatus to determine localized nano-mechanical properties (hardness, modulus of elasticity, and friction) of cross-sectioned injector parts. A series of tests were conducted that enabled us to quantify surface mechanical and friction properties of the two injector materials. Surface properties were determined with a 200-nm-radius diamond tip mounted to a precision transducer, both before and after hydrogen exposure. In addition, AFM and precision profilometry were deployed to characterize surface topography.

A JEOL scanning electron microscope (SEM) with an X-ray energy dispersive spectrometer (EDS) and attached Cambridge backscattered electron detector was used to characterize surface topology and elemental constituents.

Samples were exposed to hydrogen by including these samples in the autoclave pressure vessel at the same time piezo actuator tests were conducted.

Images in Figures 1 and 2 show the pressure vessel apparatus. These samples were placed in steel cups and exposed for the following schedule:

- 21 h at 2850 psi ambient temperature
- 5 h at 4500 psi ambient temperature
- 21 h at 4500 psi 100°C

Figure 1. High-pressure autoclave and control systems.

Figure 2. High-pressure autoclave in open position.

Samples were removed from the vessel after 47 h and stored in liquid nitrogen until tests were performed.

Results and Discussion

Surface Analysis of Injector Materials

Both designs were imaged via SEM with EDS analysis, and the surface roughness was characterized using both AFM and a Taylor-Hobson profilometer.[6]

Generally, the J2 surface was non-uniform. Areas along the needle and nozzle exhibit a more uniform surface roughness (Table 2) than the transition area of the nozzle, which contains several severe pits that EDS indicates have large portions of copper. The S1 surface is very uniform, with the roughness of the impact zone exhibiting fewer machine marks than the middle of the needle-nozzle sliding surface (Table 2). The roughness of each nozzle is highly dependent upon the location of the measurement.

Table 2. Output of surface roughness from Taylor–Hobson profilometer

Part number	Description	Ra (μm)	Slope (degrees)
A. J2	Nozzle—short end, near impact zone	0.16	–2.75
B. J2	Nozzle—transition	0.16	–1.40
C. J2	Nozzle—long end, near top of injector	0.04	–0.42
A. S1	Nozzle—middle	0.19	–0.12
B. S1	Nozzle—end	0.07	–0.58
C. S1	Needle—middle	0.19	–0.34
D. S1	Needle—end	0.06	–2.04

Figure 3 illustrates the surface of the S1 injector seat depicted in both the AFM and SEM images (top and bottom, respectively). Machine marks are clearly visible on the surface; the peak-to-peak distance is approximately 6 μm, with a surface RMS reported in the AFM image of 87 nm. The entire surface RMS is between 80 and 100 nm. EDS analysis (not shown) indicates constituents typical of carburizing steel.

Figure 4 indicates the surface topography of the S1 nozzle before exposure to hydrogen, with clearly defined machine marks. Figure 5 indicates the S1 needle after hydrogen exposure and the surface facets that formed in a localized region.

The J2 surface appears to have been pitted by the effects of corrosion at the end of the needle/nozzle impact zone (Figure 6). The SEM image of the nozzle seat illustrates the severity of the condition (scale bar at the lower left of the image is 200 μm). Pits vary in size, with an apparent depth of up to several microns.

The EDS analysis clearly indicates there is a high concentration of copper on the surface, as high as 30 wt % in some cases. The origin of this copper, we surmise, is the plating process, although we cannot be certain. It will have an adverse effect on both the performance and long-term stability of the injector.

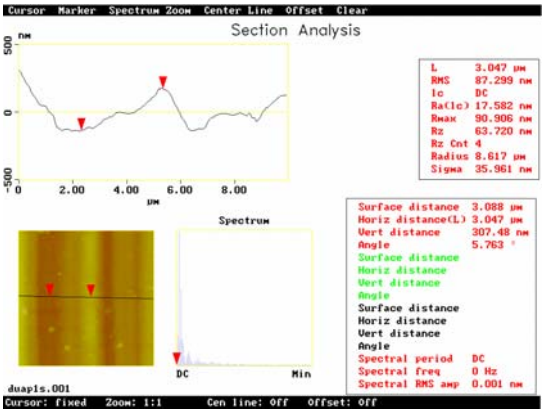

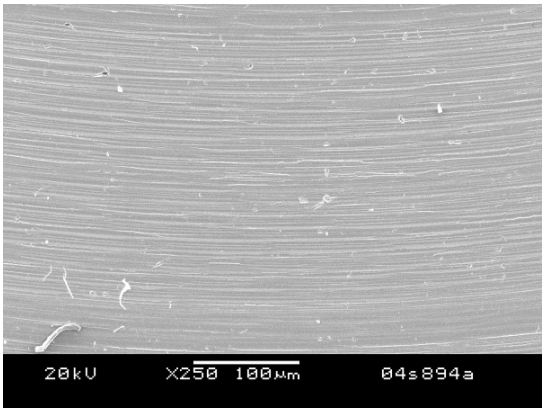

Figure 3. S1 Seat AFM image (top) and SEM image (bottom). Surface exhibits an RMS roughness of 87.3 nm, Ra = 17.52 nm, striations of approximately 6 µm peak-to-peak. EDS results indicate the primary material constituent is iron.

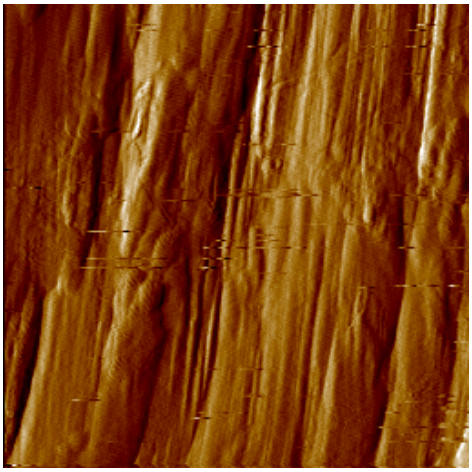

Figure 4. S1 nozzle image obtained with a scanning diamond tip via the Hysitron Nanoscratch® instrument. The image is not as clear as a true AFM, but it indicates nanoscale features. The image is 13×13 µm.

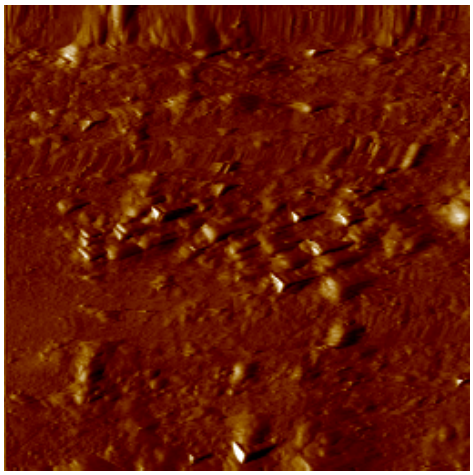

Figure 5. An S1 needle after exposure to hydrogen. The image indicates repeatable crystallites/facets on the surface, although they appear in a localized region. The image size is 13×13 µm.

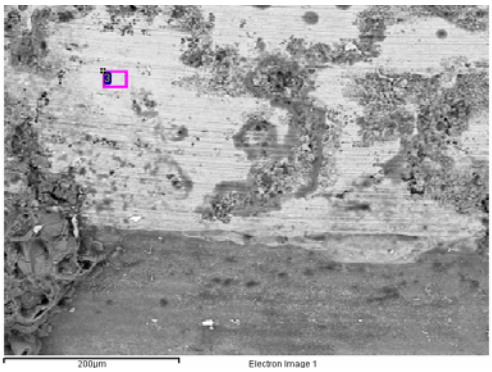

Element	Weight%	Weight % Std. dev	Atomic %
Si K	0.81	0.11	1.63
V K	0.92	0.11	1.02
Cr K	5.13	0.16	5.59
Fe K	73.84	0.47	74.94
Cu K	17.97	0.40	16.03
Mo L	1.34	0.29	0.79
Totals	100.00		

Figure 6. SEM/EDAX results from the J2 nozzle. Note the surface pitting due to corrosion; image scale bar is 200 µm.

Images of the hydrogen-exposed surfaces reveal unique features that developed. Figure 7 showing the J2 needle indicates that faceting features consistently formed across the surface.

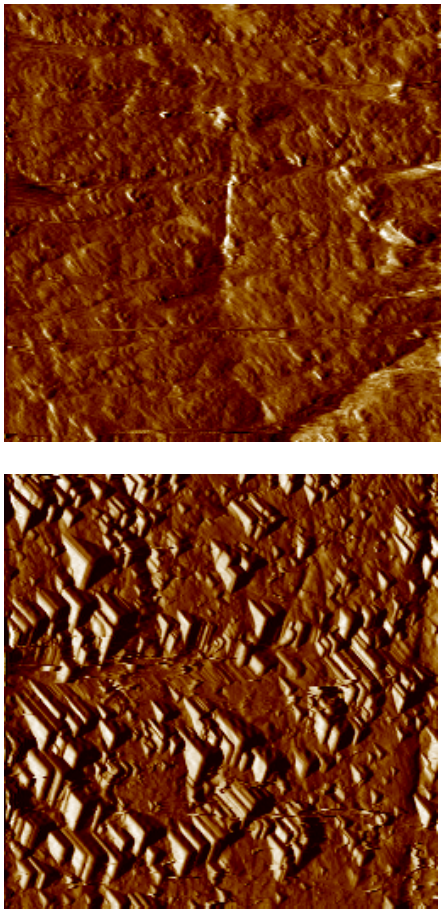

Figure 7. Images depict the J2 needle, both as-received (top) and after 47-h hydrogen exposure (bottom). Images are 25×25 μm. Peak height maximum is 4–5 μm.

These features need to be investigated further, using high-resolution SEM and TEM combined with field ion beam spectroscopy to verify the composition. Similar features, although far less dense, appear in Figure 8 on the J2 nozzle.

Figure 9 illustrate EDS images of the J2 needle with particular emphasis on the facet structure, which appears to be a combination of molybdenum and tungsten. This implies formation of molybdenum (5% in AISI M2 steel) and tungsten (6.25% in AISI M2, WCC coating) occurs under these test conditions.

Nanoindentation

Nanoindentation measurements were performed in similar areas of the S1 and J2 needle and nozzle. Table 3 is a compilation of the measurements taken.

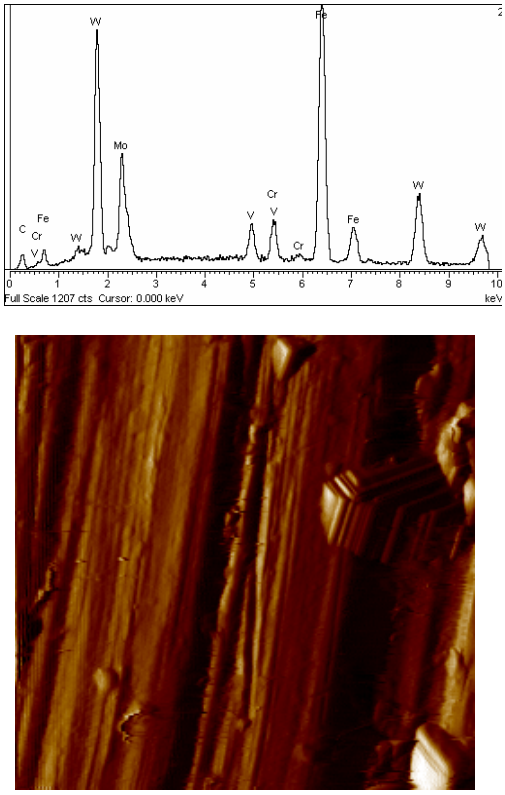

Figure 8. This image of the J2 nozzle illustrates a layered faceted feature formation on the surface after exposure to hydrogen. Image size is 15×15 μm.

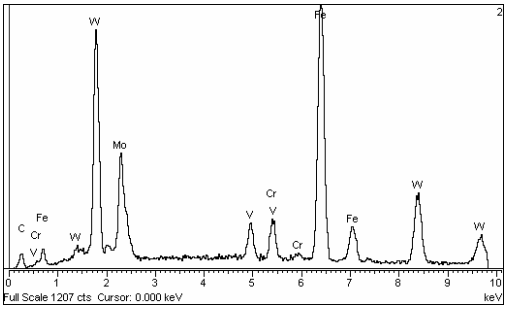

Figure 9. EDS of J2 needle surface after hydrogen exposure. The EDS plot reflects the elemental constituents in accurate proportions.

Distinct differences are a result of the effect of hydrogen exposure on each material surface. As an example, the S1 nozzle shows a distinct decrease in modulus as the result of hydrogen exposure; however, hardness shows a less dramatic effect. The correlation with friction will be addressed in the next section.

Table 3. Surface mechanical properties of the S1 and J2 needle-nozzle area. Each zone was measured with 9 indents, each indent in a 3×3 grid, a minimum of 5 mm apart.

Sample	Er (GPa)	Std. dev.	H(GPa)	Std. dev.
S1-needle	197	11.6	11.2	1.0
S1-H_2 needle	214	34.4	15.8	4.3
S1-nozzle	107	28.9	3.2	0.6
S1-H_2 nozzle	42	17.5	2.5	0.3
J2-needle	178	16.1	7.9	0.8
J2-H_2 needle	190	16.0	8.2	1.7
J2-nozzle	-	-	-	-
J2-H_2 nozzle	216	30.1	13.0	2.1

Friction Measurements

Friction measurements were generated using a Hysitron Nanoscratch apparatus fixed with a 200-nm radius diamond tip. Scratch testing represents a test form where some degree of controlled abrasive wear or adhesion between one material medium and another can be quantified under controlled conditions. In conventional scratch testing, a diamond stylus is drawn across a sample under either a constant or progressively increasing normal load; in these experiments, a constant load was employed. While the test can be used to measure the adhesion of a coating to a substrate, in these tests, we used the technique to measure the friction coefficient between the stylus and surface and, more important, to measure the change of friction under repeated stylus-surface passes.

Friction coefficient is determined from Amoton's First Law, which indicates that friction coefficient is defined as lateral force divided by the normal force as follows:

$$\mu = F_L/F_N.$$

Findings: Single-pass measurements

Single-pass friction measurements were performed on all samples. The measurements indicate differences as a function of material and exposure to hydrogen. A single-pass test, depending upon the load, will leave a scribe mark on the surface, as depicted in Figure 10. The applied normal force will dictate the amount of material removed from the scratch track.

A summary of the friction coefficient of each material tested is in Table 4. Figure 11 illustrates the friction coefficient of the S1 nozzle in "as-received" condition. The data output of 10 tests on the S1 as-received nozzle is illustrated in Figure 12. The estimated friction coefficient is 0.39.

Findings: Multi-pass measurements

A multi-pass measurement technique was developed in the course of this project. This entailed programming the Hysitron Nanoscratch instrument to perform repeated, lateral passes at a constant load to model the sliding friction between the needle and nozzle. Because of time constraints, we were able to perform only sets of 20 passes; complete results are listed in Table 5. Tests were performed with a diamond stylus, and the actual friction between needle-nozzle may behave differently. Multi-pass tests were conducted on all surfaces at a constant load; on some materials, the friction coefficient was

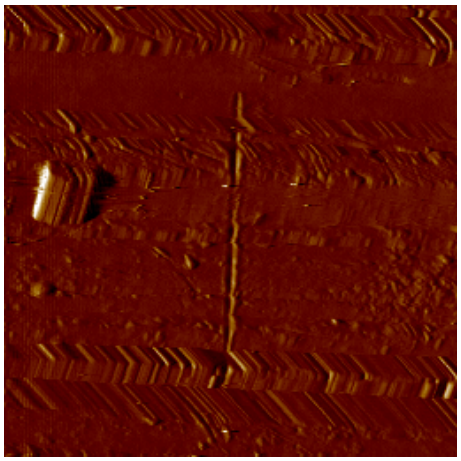

Figure 10. Single scratch on S1 nozzle after exposure to hydrogen. Image is 15×15 μm. Note the facet formation on the left of the scratch.

Table 4. Summary of the friction coefficient values of both J2 and S1 samples.

Material	Friction coefficient
J2-needle as-received	0.24
J2-needle hydrogen exposed	0.26
J2-nozzle as-received	0.18
J2-nozzle hydrogen exposed	0.27
S1-needle as-received	0.22
S1-needle hydrogen exposed	0.30
S1-nozzle as-received	0.34
S1-nozzle hydrogen exposed	0.39

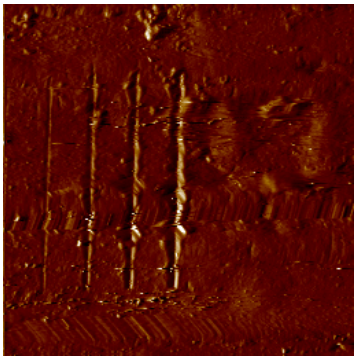

Figure 11. S1 needle scratch pattern. Image is 15×15 μm. Several scratches were made on the sample at various loading conditions.

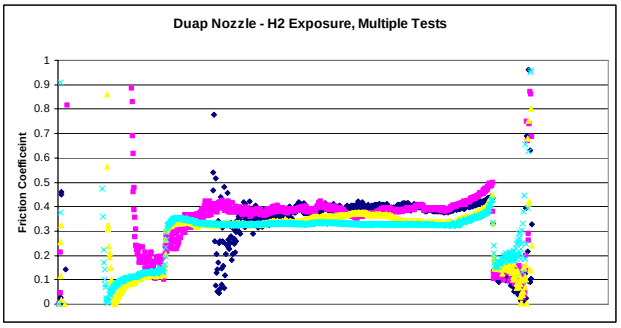

Figure 12. Comparison of the S1 nozzle friction coefficient in as-received condition. These are four plots taken at 250 mN. Friction coefficient is estimated to be 0.39.

Table 5. Summary of the multi-pass friction coefficient values of both J2 and S1 samples

Material	Friction coefficient
J2-needle as-received	0.53*
J2-needle hydrogen exposed	0.51*
J2-nozzle as-received	0.55
J2-nozzle hydrogen exposed	0.73*
S1-needle as-received	0.45
S1-needle hydrogen exposed	0.58
S1-nozzle as-received	0.53
S1-nozzle hydrogen exposed	0.68

* One sample data point; additional test necessary.

constant, while on others the friction coefficient in creased with each successive pass. This likely indicates that the diffusion rate of hydrogen is quite different in the materials tested, as well as the change in surface hardness as a function of penetration.

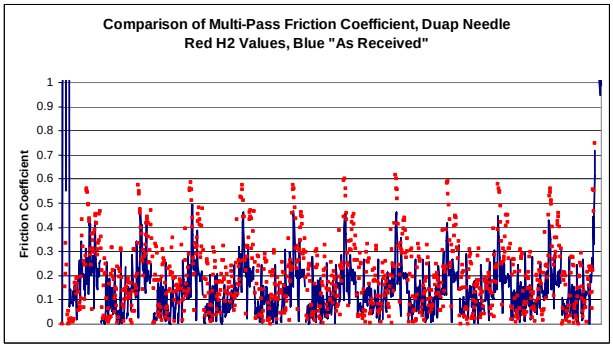

Figure 13. Multi-pass measurement of the S1 needle, both as-received (solid line) and after hydrogen exposure (dots). The friction coefficient is estimated to increase by 0.13 as a result of the hydrogen exposure.

For example, Figure 13 indicates that the S1 needle multi-pass experiment is relatively constant, regardless of the exposed condition. While the overall friction coefficient increased by 0.13, the value of each condition was constant. On the other hand, a multi-pass measurement on the J2 nozzle in the as-received condition reveals that there is an increase in friction coefficient with each successive pass. Perhaps this increase in friction coefficient is due to the removal of material resulting in greater depth of penetration and subsequently more and more surface oxides and hydrogen-exposed materials removed.

In the course of this project, Pacific Northwest National Laboratory (PNNL) researchers in conjunction with Oak Ridge National Laboratory researchers established nano- and micro-scale techniques to measure the friction of sliding hydrogen injector interfaces. Using a hydrogen-specific pressure vessel developed at PNNL during the course of this project, injector materials supplied by Westport Innovations were exposed to 47 h in a pressurized hydrogen environment, and the surfaces were subsequently analyzed using SEM, EDS, AFM, nanoindentation, and nanoscratch techniques. A summary of the material properties tested is provided in Table 6.

Material surface phenomena were discovered on the surfaces that appear to be the result of facet formation composed of a molybdenum-tungsten compound. They range from 100 nm to 5 μm in diameter and up to 4 μm in height. At this time, the structure is not well defined, and the rate of

Table 6. Summary of friction coefficient and surface property data of J2 and S1 samples. (*) indicates one sample data point.

Sample	Er (GPa)	H (GPa)	Friction coefficient	Multi-pass friction	Comments
S1 needle as-received	197	11.2	0.22	0.45	
S1 needle hydrogen exposed	214	15.8	0.30	0.58	
S1 nozzle as-received	107	3.2	0.34	0.53	No facets prior to hydrogen
S1 nozzle hydrogen-exposed	42	2.5	0.39	0.68	Facets present
J2 needle as-received	178	7.9	0.27	0.53*	
J2 needle hydrogen exposed	190	8.2	0.26	0.51*	Facet formation
J2 nozzle as-received	–	–	0.18	0.55	Copper present

evolution is not understood. Further research is required to determine the nature of the crystal formations; the lamellar nature will require structural analysis to determine their exact impact on sliding surfaces.

Industrial samples analyzed in the course of this study showed various degrees of contamination including copper and other species. The surface roughness *Ra* of the samples was between 0.03 and 0.16 μm, with friction coefficients determined using a 200-nm radius diamond tip. Hydrogen exposure appears to increase slightly the friction coefficient of all materials. The S1 materials showed increases in single-pass tests of up 0.08 and 0.05 for the needle and nozzle, respectively. Given that the only decrease in friction coefficient was determined on the J2 needle, which maintained the greatest distribution of facet formation, we believe the formation of these facets may assist in stabilizing the friction coefficient of the surface. This trend was also present in the case of the multi-pass testing, although with only a single data point. Further testing is necessary to better understand this material characteristic.

Multi-pass friction testing indicates that for the S1 materials—the only set fully tested with the technique developed herein—under a 100-mN load, the friction coefficient increases by 0.13 and 0.15 for the needle and nozzle, respectively. Further testing and characterization is needed to support our findings. This will require a dedicated effort and will include model sample substrates that will add to the body of data created thus far on industrial samples.

References

1. W.P. Chen, X.P. Jian, Y. Wang, Z. Peng, H.L.W. Chan, "Water-Induced Degradation of Barium Titanate Ceramics Studied by Electrochemical Hydrogen Charging," *J. of the American Ceramic Society* **86** (4), 735–737 (April 2003).
2. T. Shimada, C. Wen, N. Taniguchi, J. Otomo, H. Takahashi, "The High-Temperature Proton Conductor BaZr0.4Ce0.4In0.2O3-alpha," *J. of Power Sources* **131** (1–2), 289–292 (May 14, 2004).
3. D.J. Jung, F.D. Morrison, M. Dawber, H.H. Kim, K. Kim, J.F. Scott, "Effect of Microgeometry on Switch and Transport in Lead Zironcate Titanate Capacitors: Implications for Etching of Nano-Ferritics," *Journal of Applied Physics* **95** (9), 4968–4975 (May 1, 2004).
4. Y. Wang, X. Peng, W.Y. Chu, Y.J. Su, L.J. Qiao, K.W. Gao, "Anisotropy of Hydrogen Fissure and Hydrogen-Induced Delayed Fracture of a PZT Ferroelectric Ceramic," in *Proceedings of the 2nd International Conference on Environment Induced Cracking of Metals*, October 2004, Banff, Canada, in press.
5. W.F. Stockhausen, R.J. Natkin, D.M. Kabat, L. Reams, X. Tang, S. Hashemi, S.J. Szwabowski, V.P. Zanardelli, "Ford P2000 Hydrogen Engine Design and Vehicle Development Program," SAE 2002-01-0240, SAE World Congress, Detroit, March 4–7, 2002.
6. J.D. Holbery et al., "High-Pressure Hydrogen Effect on Sliding Contact Surfaces," MRS paper Y9.4, MRS Fall Meeting, Boston, November 28–December 2, 2005.

E. Advanced Materials Development through Computational Design for HCCI Engine Applications

Vinod K. Sikka, G. (Murali) Muralidharan, and Paul C. Becker
Metals and Ceramics Division
(865)574-5112;, fax: (865) 574-4357; e-mail: sikkavk@ornl.gov
Bruce G. Bunting
Engineering Science and Technology Division
(865) 946-1512; fax: (865) 946-354;, e-mail: buntingbg@ornl.gov

DOE Materials Technologies Team Leader: Rogelio Sullivan
(202) 586-8042; fax: (202) 586-1600; e-mail: rogelio.sullivan@ee.doe.gov
ORNL Technical Advisor: David Stinton
(865) 574-4556; fax: (865) 241-0411; e-mail: stintondp@ornl.gov

---

Contractor: Oak Ridge National Laboratory, Oak Ridge, Tennessee
Prime Contract No.: DE-AC05-00OR22725

Objectives

- Identify and catalog the materials operating conditions in homogeneous charge compression-ignition (HCCI) engines and use computational design concepts to develop advanced materials for such applications.
- Interact with designers of HCCI engines and manufacturers of components in order to identify the components that will be affected by the harsh operating conditions resulting from the HCCI design.
- Identify the highest-priority component(s) that are critical to the implementation of the HCCI concept.

Approach

- Identify engine components, currently used materials, and current operating conditions and compare them with the expected component operating conditions for HCCI engines.
- Demonstrate the feasibility of the “materials by design” approach for the highest-priority item. Improve material performance for HCCI application through computational modeling and experimental validation.

Accomplishments

- Based on discussion with seven automotive and truck companies, identified four improved materials needs/opportunities in support of advanced engine concepts such as HCCI [i.e., aluminum for charge air coolers, cast irons for exhaust manifolds, nickel (Ni) alloys for exhaust valves, and alloy steels for fuel injectors].
- Identified opportunities for leveraging DOE funds. Collaborations have been established with two companies to work on two of the materials needs.
- Completed initial calculations of materials development through computational design for Ni-based alloy compositions. The weight percent of γ' shows a qualitative agreement with published fatigue data.

Future Direction

- Communicate with automotive companies, Diesel Cross-Cut Team, FreedomCAR, and 21st Century Truck on the progress made through computational design.
- Develop correlation of phases with properties.

Introduction

There has been an increasing interest in HCCI combustion in recent years because of its potential to increase engine combustion efficiency and reduce emissions. However, the use of HCCI combustion will subject the engine components to significantly higher temperatures and pressures. The temperatures for diesel engines will reach over 1600°F, and pressure may reach > 2000 psi, which is approximately four times that of the normal combustion engine. Such severe engine operating conditions will require a significant improvement in materials performance in order to take advantage of the HCCI engine concept. This project deals with identifying materials requirements for HCCI engines for automotive and truck applications and the development of advanced, yet cost-effective materials through computational design.

"Materials by design" is an Oak Ridge National Laboratory (ORNL) concept and collection of materials-related techniques involving modeling, correlation, and materials modification. The premise behind materials by design is that mechanical properties are correlated to microstructure and phase chemistry. The phase composition and microstructure can be achieved through thermodynamic equilibrium or through non-equilibrium techniques such as quenching, rapid casting solidification, or mechanical working. These characteristics can then be correlated to desired mechanical properties through equilibrium thermodynamics or through a variety of correlation techniques. These correlations or modeling allow untested compositions or treatments to be modeled so that desired trends can be rapidly established. Small heats of targeted materials can then be processed to confirm the modeled properties and to broaden the correlation data base.

Finally, there are several techniques such as magnetic processing or low-temperature carburizing that can be applied to allow further modification and optimization of desired properties. Materials by design is ideally suited to cast and heavily thermally processed materials such as stainless steels, Ni alloys, cast irons, alloy steels, and brazed wrought aluminum alloys and has been successfully applied in such diverse areas as high-temperature furnace components, exhaust valves, exhaust manifolds, and tube fittings. Figure 1 and Table 1 provide an outline of the materials by design approach and a summary of the techniques that can be applied.

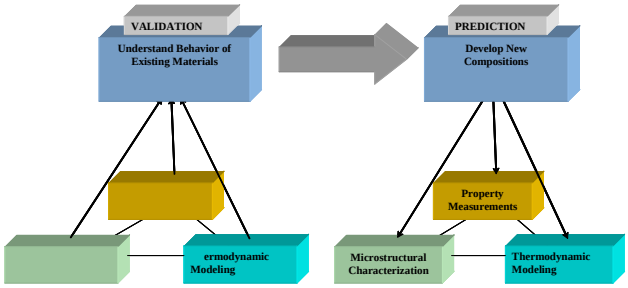

Figure 1. Overall approach for Materials by Design.

In our approach, we examined critical heavy-duty diesel engine materials and identified means to reduce their cost for acceptance in HCCI applications. This was accomplished through the following tasks:

Task 1. Identify critical material requirements for HCCI engines based on their operating conditions. The outcome of this task will be accomplished through interactions with advanced engine and component designers. The interactions will include personal visits to six companies: Caterpillar, Cummins Engine, Deer, International Truck, Eaton Corp., and General Motors. Visits will be supplemented by literature search, review of advanced engine design studies, and further discussion following the visits. The key outcome from this task will include (1) identifying operating conditions for advanced engine concepts with a focus on the HCCI concept; (2) identifying components most affected by these operating conditions; (3) identifying currently used materials, new requirements, and performance targets; and (4) ranking the highest-priority items for study by the materials by design approach.

Table 1. ORNL Materials by Design toolbox

ORNL Materials by Design Toolbox		
Modeling	Experimentation	Characterization
Thermodynamic modeling of material properties vs alloy composition	Ultra-high-gauss magnetic stabilization of alloy steels	Advanced microscopy techniques
Neural-network modeling of diverse, nonlinear materials properties and process variations	Low-temperature gas carburization of finished components	X- ray and neutron scattering Surface and bulk property measuring techniques
Detailed microstructure based empirical modeling	Ability to produce small quantities of materials and fabricate them into test bars for property measurements and production of prototype components by a variety of methods, including sand and die casting, extrusion, forging and rolling	
Non-equilibrium modeling of solidified structures		
Extrapolation of properties from simple alloy systems to complex systems using interaction parameters		

Task 2. Demonstrate the feasibility of materials by design approach for the highest-priority item. In this task, we will identify the details of the currently used material for the highest-priority item. This will include material compositions, processing methods, mechanical properties, corrosion properties, and cost.

Based on the available mechanical properties data, microstructural analysis, and thermodynamic phase stability calculations, we will identify the underlying mechanism that delivers the current properties.

Task 3. Improve material performance for HCCI application through computational modeling and experimental validation. In this task, we will use computational modeling (key basis for the material by design concept) to identify compositions that will deliver the desired phases for two purposes: improving the property performance and finding alternatives to reduce cost for current and improved performance. The outcome of the analysis will be validated through experimentation. The validation will be carried out in the following steps:

1. Prepare compositions identified based on computational design in 1-lb heats for microstructural analysis and very limited property determination; compare the results with output based on computational analysis for validation.
2. Scale up the validated composition into 20- to 100-lb heats and cast them into ingots for processing trials. In most cases, the material is expected to be used in the wrought condition. However, if it is to be used in the cast condition, we will save part of the ingots for analysis of as-cast properties.
3. Subject cast ingots to processing steps that are currently used by industry. Develop optimum processing and heat-treatment conditions to obtain the desired microstructure.
4. Carry out microstructural analysis and mechanical properties analysis on the material processed and heat-treated with optimum conditions.
5. Prepare autotype components for HCCI engine tests.

A strong interaction with industrial partners will occur during all three tasks. This interaction is expected to result in the rapid transfer of materials improvement from this project to industry for use in HCCI and other advanced engine concepts.

Results

The scope of this project was presented to the Diesel Cross-Cut Team that represents experts from the FreedomCAR and 21st Century Truck programs. Seven companies were interviewed. The companies interviewed, their business, and type of interview are summarized in Table 2. The following needs and opportunities were identified based on the interviews to date:

1. High-strength, thermally stable, corrosion-resistant aluminum for charge air coolers.
2. Optimization of Ni alloys for exhaust valves to reduce cost, extend high-temperature performance, and improve high-temperature fatigue life.
3. For cast irons, effect of alloying elements on cost, high-temperature capability, and greater crack resistance under temperature and stress cycling.
4. Wear-resistant, higher-strength, higher-temperature, capable alloy steels for fuel injection components.

Table 2. List of companies interviewed.

Company	Business	Type of interview
Cummins	Diesel engines	Meeting at ORNL
Caterpillar	Diesel engines, off-road equipment	Meeting at Caterpillar plus white paper
International	Engines and vehicles	E-mail interviews
MIT Sloan Automotive Lab	Engine and Combustion reserach	Off-site meeting
General Motors Powertrain	Vehicle manufacturing	Meeting at GM
Eaton	Valves and value train components, EGR	Meeting at Eaton
Delphi Diesel Systems (formerly Lucas)	Diesel fuel injection	Off-site meeting

Most of the needs identified are not show-stoppers; but opportunities for significant improvements are available through incremental advances in materials, and research capability at ORNL can help speed this process. We have also identified leveraging opportunities for funds-in projects or substantial cost share with interviewees in the areas of cast exhaust manifolds and Ni alloy use for exhaust valves. There is an opportunity for additional interaction with industry through new DOE-funded high-efficiency clean combustion partnerships.

In addition to the materials needs listed earlier, comments from our interactions with interviewees indicated that light-duty truck needs are not the same as heavy-duty truck concerns. The specific differences are listed in Table 3.

Table 3. Differences in needs for heavy- and light-duty trucks

Heavy duty	Light duty
Heavy-duty engines are designed to run at full load a large portion of time with an average load factor of up to 70%.	Light-duty engines are designed to run at full load only briefly and operate with an average load factor of about 20%.
Emissions certification for heavy duty requires steady state full-load operation.	Emissions certification for light duty is done using a simulated driving cycle with brief full-load operation.
Heavy-duty engine designers are concerned mainly about structural integrity and fuel efficiency; noise is secondary .	Light-duty engine tuning is restrained by limits for engine harshness and noise.
Heavy-duty engines use higher-performance, more expensive materials today.	Heavy-duty materials could trickle down to light duty if needed.
Heavy-duty manufacturers know they need higher-performance materials.	Light-duty manufacturers are currently studying lighter-weight, lower-cost materials, such as plastics, to see if HCCI will enable their use due to lower temperatures and less radiant heat transfer.

Initial Results from Materials Development through Computational Design

As a first step to materials development through the computational design approach, phase equilibrium calculations were carried out on published candidate compositions of Ni-based alloys. The alloys used for calculations were 70Ni-19Cr, IN751, and Nimonic 90A. An example of the phase equilibrium for IN751 [Ni-1.23-1.0Co-15.5Cr-7.0Fe-0.5Mn-0.45Nb-0.5Si-0.5Ta-2.3Ti-0.5W (at. %)] is shown in Figure 2. This plot shows the weight percent of various phases and their stability as a function of temperature. The γ′ phase in Ni-based alloys is considered to control their properties. The relative weight percent and the stability of γ′ for the three alloys investigated are shown in Figure 3. There is less γ′ in IN751, and it is stable only up to approximately 830°C. The other

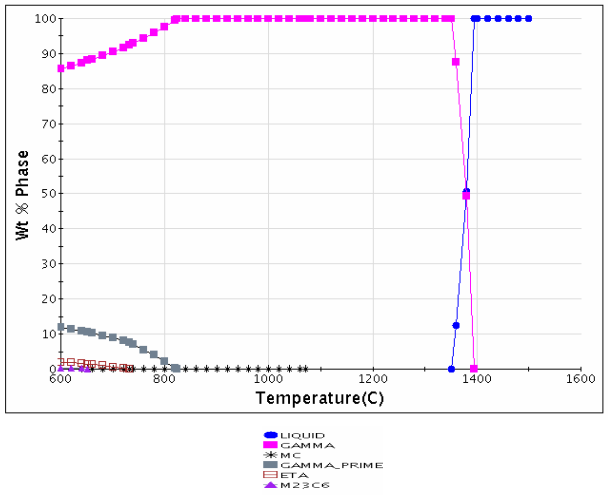

Figure 2. Phase equilibria in IN751.

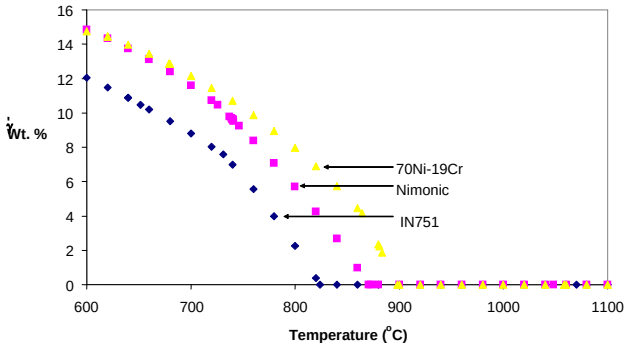

Figure 3. Comparison of weight percent γ′ in three Ni-based alloys.

two alloys have higher amounts of the γ′ phase, and they are stable to higher temperatures.

Published data on fatigue properties of several alloys are shown in Figure 4. Comparison of the γ′ phase in Figure 3 with Figure 4 shows that there is a qualitative agreement between the weight percent of γ′ and the fatigue properties (i.e., IN751 with the lowest weight percent of γ′ has lower fatigue strength than alloy 70Ni-19Cr, which has the highest weight percent of γ′ (Figure 2).

Work will continue to quantify the correlation between fatigue properties and phase type, and weight percent will be validated on experimental-size heats of selected compositions. Results of this study will be shared with the industrial partner.

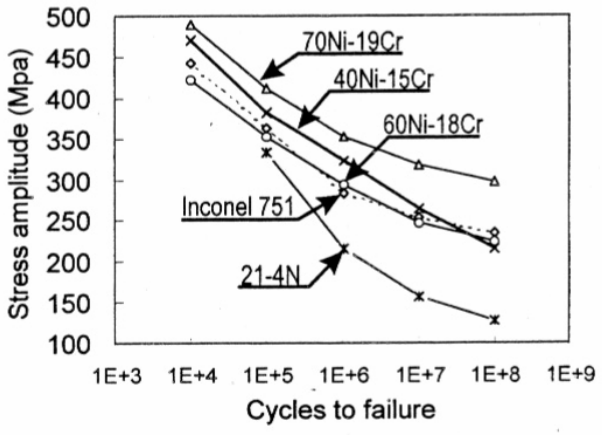

Figure 4. Comparison of fatigue properties of IN751 and 70Ni-19Cr with various alloys.[1]

Conclusions

Seven automotive and truck companies were contacted. Based on discussions with these companies, four materials improvement needs and opportunities were identified in support of advanced engine concepts such as HCCI.

Initial calculations of materials development through computational design were completed for three published Ni-based alloy compositions. The weight percent of γ′ phase shows a qualitative agreement with the published fatigue data for two of the three alloys used in the calculations.

References

1. K. Sato, Y. Takagi, and T. Saka, “The Progress of Valvetrain Design and Exhaust Valve Material Research for Automobiles,” in

Proceedings of the International Symposium on Valvetrain System Design and Materials.

Publications/Presentations

Vinod K. Sikka, Govindarajan Muralidharan, Paul C. Becker, and Bruce Bunting, "Materials for HCCI: A Materials by Design Approach," presentation to Rogelio Sullivan of DOE, at ORNL, May 5, 2005.

Vinod K. Sikka, Govindarajan Muralidharan, Paul C. Becker, and Bruce Bunting, "Materials for HCCI: A Materials by Design Approach (Revised on June 20, 2005)," presentation to Diesel Cross-Cut Team, at ORNL, July 21, 2005.

APPENDIX A: ACRONYMS AND ABBREVIATIONS

AFM	atomic force microscopy
ANL	Argonne National Laboratory
ANL–ES	ANL–Energy Systems
APS	Advanced Photon Source
APM	Automotive Propulsion Materials
ASTM	American Society for Testing and Materials
CIDI	compression-ignition direct-injection
DOE	U.S. Department of Energy
DPF	diesel particulate filter
DSC	differential scanning calorimetry
EDM	electrodischarge machining
EDX	energy-dispersive X-ray spectroscopy
EE	Electrical and Electronics
EGR	exhaust gas recirculation
EN	electroless nickel
EPA	Environmental Protection Agency
EPA–NVFEL	EPA National Vehicle and Fuel Emissions Laboratory
EXAFS	X-ray absorption fine structure
FCVT	FreedomCAR and Vehicle Technologies
ffm	friction force microscopy
FTP	Federal Test Protocol
FY	fiscal year
H	hardness
H^+	hydrogen ion
H_2	hydrogen gas
H2RV	hydrogen hybrid research vehicle
HCCI	homogeneous charge compression-ignition
I-V	current-voltage
ICS	Industrial Ceramic Solutions
ID	internal diameter
ITO	tin-doped indium oxide
LANL	Los Alamos National Laboratory
L/D	length-to-diameter
LLNL	Lawrence Livermore National Laboratory
LSC	$LaCoO_3$
MEA	membrane electrode assembly

NdFeB	neodymium-iron-boron
Nd	neodymium
Ni	nickel
NIST	National Institute for Standards and Testing
NIU	Northern Illinois University
nm	nanometer, 10^{-9} meters
NO	nitrogen oxide, nitric oxide
NO_x	oxides of nitrogen
NVFEL	National Vehicle and Fuel Emissions Laboratory
OEM	original equipment manufacturer
OFCVT	Office of FreedomCAR and Vehicle Technologies
ORNL	Oak Ridge National Laboratory
Pd	palladium
PM	permanent magnet or particulate matter
PNNL	Pacific Northwest National Laboratory
PPS	polyphenylene sulfonate
Pt	platinum
PVOH	hydroxylated polystyrene
PZT	lead zirconium titanate
R&D	research and development
S	sulfur
Sr	strontium
SAE	Society of Automotive Engineers
SEM	scanning electron microscope/scanning electron microscopy
SNL	Sandia National Laboratories
T	Tesla
TGA	thermogravimetric analysis
WC	tungsten carbide
XPS	X-ray photoelectron spectroscopy
XRD	X-ray diffraction
YSZ	yttria-stabilized zirconium

A Strong Energy Portfolio for a Strong America

Energy efficiency and clean, renewable energy will mean a stronger economy, a cleaner environment, and greater energy independence for America. Working with a wide array of state, community, industry, and university partners, the U.S. Department of Energy's Office of Energy Efficiency and Renewable Energy invests in a diverse portfolio of energy technologies.

For more information contact:
EERE Information Center
1-877-EERE-INF (1-877-337-3463)
www.eere.energy.gov